ARTICLE

# Constructing Double Heterojunctions on 1T/2H-MoS₂@Co₃S₄ Electrocatalysts for Regulating Li₂O₂ Formation in Lithium-Oxygen Batteries

Yichuan Dou[1,4], Zhuang Liu[1,4], Lanling Zhao[2] ✉, Jian Zhang[3], Fanpeng Meng[3], Yao Liu[1,4], Zidong Zhang[1,4], Xingao Li[2], Zheng Shang[2], Lu Wang[2], Jun Wang[1,4] ✉

HIGHLIGHTS

- 1T/2H-MoS₂@Co₃S₄ electrocatalysts were constructed by interfacial charge donation from Co to Mo atoms, resulting in formation of double heterojunctions including 1T-MoS₂@Co₃S₄ and 2H-MoS₂@Co₃S₄.

- Complementary effect from double heterojunctions not only triggered fast charge transport on Co–S–Mo couplings, but also enabled moderate e_g orbital occupancy to adsorb oxygen-containing intermediates for efficient oxygen electrocatalysis.

- Optimal adsorption energies for solution and surface dual reaction pathways were achieved, forming two kinds of discharge product morphologies during cycling to enhance performance of Li–O₂ batteries.

ABSTRACT Co₃S₄ electrocatalysts with mixed valences of Co ions and excellent structural stability possess favorable oxygen evolution reaction (OER) activity, yet challenges remain in fabricating rechargeable lithium-oxygen batteries (LOBs) due to their poor OER performance, resulting from poor electrical conductivity and overly strong intermediate adsorption. In this work, fancy double heterojunctions on 1T/2H-MoS₂@Co₃S₄ (1T/2H-MCS) were constructed derived from the charge donation from Co to Mo ions, thus inducing the phase transformation of MoS₂ from 2H to 1T. The unique features of these double heterojunctions endow the 1T/2H-MCS with complementary catalysis during charging and discharging processes. It is worth noting that 1T-MoS₂@Co₃S₄ could provide fast Co–S–Mo electron transport channels to promote ORR/OER kinetics, and 2H-MoS₂@Co₃S₄ contributed to enabling moderate e_g orbital occupancy when adsorbed with oxygen-containing intermediates. On the basis, the Li₂O₂ nucleation route was changed to solution and surface dual pathways, improving reversible deposition and decomposition kinetics. As a result, 1T/2H-MCS cathodes exhibit an improved electrocatalytic performance compared with those of Co₃S₄ and MoS₂ cathodes. This innovative heterostructure design provides a reliable strategy to

---
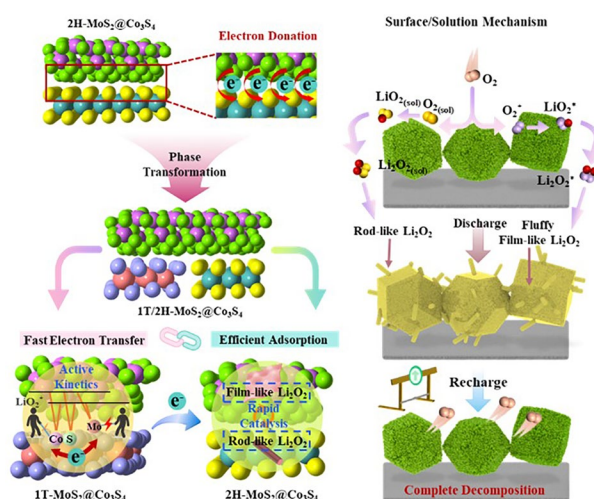
Yichuan Dou and Zhuang Liu have contributed equally to this work.

✉ Lanling Zhao, lanling@sdu.edu.cn; Jun Wang, jw707@sdu.edu.cn

[1] Key Laboratory for Liquid-Solid Structural Evolution and Processing of Materials (Ministry of Education), Shandong University, Jinan 250061, People's Republic of China

[2] School of Physics, Shandong University, Jinan 250061, People's Republic of China

[3] Shandong Guiyuan Advanced Ceramics Co., Ltd, Zibo 255020, People's Republic of China

[4] Shandong Key Laboratory of Metamaterial and Electromagnetic Manipulation Technology, Jinan 250061, People's Republic of China

construct efficient transition metal sulfide catalysts by improving electrical conductivity and modulating adsorption toward oxygenated intermediates for LOBs.

KEYWORDS Double heterojunctions; d-p hybridization; Tunable Li_2O_2 deposition; Electrocatalysts; Lithium-oxygen batteries

1 Introduction

Aprotic lithium-oxygen batteries (LOBs) are one of the most promising candidates to replace lithium-ion batteries (LIBs) for electric vehicles, robots, and large-scale grids, because of their ultrahigh theoretical energy density ($3,500$ W h kg^{-1}). Generally, the reaction mechanisms during cycling are based on $Li^+ + O_2 \leftrightarrow Li_2O_2$ ($E^0 = 2.96$ V *vs.* Li/Li$^+$), which involves oxygen reduction reaction (ORR) for discharging and oxygen evolution reaction (OER) for charging [1, 2]. However, such a powerful system is greatly hindered for further applications by poor rate performance, limited cyclic life, and high overpotentials. These problems mainly result from their sluggish redox kinetics, triggering the accumulation of inactive discharge product (Li_2O_2) and even insulated side reaction product (LiOH and Li_2CO_3) on the cathode [3]. Considering that the cathodes should exposure the triple-phase contact interface regions (cathode/electrolyte/O_2) and enable discharge product storage, employing ideal cathode catalysts for fast electron transfer rate and reversible discharge product formation would greatly enhance the electrocatalytic performance and accelerate the commercial applications of LOBs.

Noble metals and their alloys exhibit high-efficiency catalytic properties in LOBs, while the high cost and scarcity on the Earth's crust seriously restrict their large-scale applications [4, 5]. Transition metal chalcogenides (TMCs) have been attracting extensive attention worldwide on account of their low cost, excellent chemically active electrocatalytic property, and diversity of structure [6]. Among them, Co_3S_4 possesses a typical spinel structure with a mixture valence state of Co^{2+} and Co^{3+}, and this unique arrangement endows Co_3S_4 eye-catching recognition as the OER electrocatalyst, proved by density functional theory (DFT) calculations [7, 8]. Liu et al. [9] synthesized ultrathin Co_3S_4 nanosheets via a sonicated treatment, delivering high OER activities and reduced overpotentials in overall water splitting reactions. Wang et al. [10] present superior manner in OER performance, which can be realized by inducing sulfur vacancies in Co_3S_4. Furthermore, Yang et al. [11] demonstrate that the adsorption states of oxygen-containing intermediates could be tailored by Ni incorporation to largely influence OER activities. However, it is proposed that the monometallic sulfides generally fail to simultaneously exhibit the high electrocatalytic activities toward bifunctional electrocatalytic reactions (ORR and OER) [12]. In fact, when exposed to ambient environment or an oxygen-containing solution, Co_3S_4 tends to be extraordinarily reactive and unstable, which is prone to rapid oxidation due to the weak Co–S bonds and results in low electrical conductivity during ORR [13, 14]. Thus, it is necessary to construct heterostructures to offer conductive support for Co_3S_4 and further achieve bifunctional electrocatalytic abilities.

As another widely studied TMCs, MoS_2 catalysts have been widely applied as one of the key alternatives to noble metal catalysts in electrochemical fields [15, 16]. It is found that MoS_2 exhibits the layered S-Mo-S sandwich structure, connected by weak van der Waals forces along the c-axis. Besides, according to the stacking manner of S atoms, there are three different crystalline phases of MoS_2, including 1T (trigonal structure, octahedral coordination), 2H (hexagonal structure, trigonal prismatic coordination), and 3R (rhombohedral structure, trigonal prismatic coordination) [17]. Due to intrinsic properties, $3R-MoS_2$ has been proven to be a promising material for optoelectronic and photonic devices [18, 19]. $2H-MoS_2$ is dominant and more stable in nature, showing the characteristics of a semiconductor with a large bandgap between 1.29 and 1.90 eV. Researchers have calculated and proven that $2H-MoS_2$ possesses ultra-low adsorption energy (E_{ads}) for reaction intermediates and hardly adsorbs the reaction intermediates, while the stack edge planes of $2H-MoS_2$ can confine reaction species and restrict growth of the discharge product due to the ultrahigh E_{ads}. To increase electrical conductivity and E_{ads} toward oxygen-containing intermediates, a variety of strategies were carried out, including hybridization with carbon materials (carbon nanotubes [20], graphene oxide [21], and other carbon materials [22, 23]), doping with heteroatoms [24, 25], and constructing S vacancies [26, 27]. The bandgap of $1T-MoS_2$ is close to zero with metallic property, exhibiting

10^7 times higher electrical conductivity than that of 2H-MoS$_2$, which is pivotal for enhancing its catalytic performance [28, 29] Theoretical calculations confirm that the octahedral coordination favors the accommodation of these extra electrons in the d orbitals of Mo atoms, gifting 1T-MoS$_2$ with metallic property [30]. However, 1T-MoS$_2$ is considered to be thermodynamically unfavorable and hard to realize high-yield production, leading to spontaneous phase reversion to 2H-MoS$_2$ [31, 32]. It is reported that electron configuration modulation for 2H-MoS$_2$ could induce 1T-MoS$_2$ formation due to the electron injection to Mo 4d, and the existence of 2H-MoS$_2$ can contribute to stabilizing 1T-MoS$_2$ [33–35]. Therefore, heterostructures based on MoS$_2$ are believed to offer a new platform to explore this connection owing to the abundant charge donation on the heterointerfaces.

Herein, ZIF-67 was employed as template to synthesize 1T/2H-MoS$_2$@Co$_3$S$_4$ heterostructures (1T/2H-MCS) as bifunctional electrocatalysts for LOBs via one-pot hydrothermal method with two-step temperature-raising process. The original electron configuration of Mo 4d orbitals was changed via the electron injection by Co 3d, which triggered the phase transition from 2H to 1T to form double heterojunctions of 1T-MoS$_2$@Co$_3$S$_4$ and 2H-MoS$_2$@Co$_3$S$_4$ in 1T/2H-MCS. According to the theoretical calculations on Co$_3$S$_4$, 2H-MoS$_2$, 1T-MoS$_2$@Co$_3$S$_4$, and 2H-MoS$_2$@Co$_3$S$_4$, the complementary effects on 1T/2H-MCS were intensively investigated. On the one hand, owing to the increasing density of states (DOS) at the Fermi energy level, 1T-MoS$_2$@Co$_3$S$_4$ exhibits excellent electrical conductivity via the fast electron transport channels of Co–S–Mo bonds, while the low E$_g$ orbital occupancy is unfavorable for adsorption of oxygen-containing intermediates, resulting from the large bandgap between d-band center (E$_d$) of Co and Fermi level. On the other hand, due to the appropriate d-p orbital hybridization of 2H-MoS$_2$@Co$_3$S$_4$ and LiO$_2$ with modulated E$_d$ of Co, 2H-MoS$_2$@Co$_3$S$_4$ shows suitable E$_{ads}$, enabling the changed adsorption configuration of oxygen-containing intermediates to efficiently adsorb and desorb the discharge product. Nevertheless, the overall electrical conductivity of 2H-MoS$_2$@Co$_3$S$_4$ is poor due to the wide bandgap of 2H-MoS$_2$. Moreover, 1T/2H-MCS could completely maintain dodecahedral hollow structure from ZIF-67 and be decorated with MoS$_2$ nanosheets. This unique 3D architecture can effectively impede the agglomeration and restack of MoS$_2$, exposing more active sites and promoting mass diffusion for faster reaction kinetics. Together with these synergistic effects, 1T/2H-MCS cathodes exhibit significantly improved electrochemical activities for both OER and ORR, including a discharge specific capacity of 16,875 mAh g^{-1} at 0.5 mA cm^{-2} with a capacity retention of up to 96% and a steady cycle life of 375 cycles at 0.5 mA cm^{-2} with a cutoff specific capacity of 1 mAh cm^{-2}, and these data demonstrate their practical application potential for next-generation high energy–density power sources.

2 Experimental Section

2.1 Synthesis of ZIF-67

The typical reaction process for the preparation of ZIF-67 template is as follows. 3 mmol cobalt nitrate hexahydrate and 12 mmol 2-methylimidazole were dissolved in 30 and 10 mL of methanol , respectively, which were then mixed and aged at room temperature for 24 h. After complete centrifugal washing with methanol, ZIF-67 product was dried at 80 °C overnight.

2.2 Synthesis of 1T/2H-MoS$_2$@Co$_3$S$_4$ (1T/2H-MCS)

50 mg of as-prepared ZIF-67 templates were added into 10 mL ethanol under sonication for 10 min. Consequently, 10 mL aqueous solution containing Na$_2$MoO$_4$·2H$_2$O (0.033 M) and thioacetamide (TAA, 0.1 M) was added slowly into the above solution under sonication for another 10 min. Afterward, the uniform mixture was placed into a 40-mL Teflon-lined stainless-steel autoclave, which was maintained at 120 °C for 4 h and then raised to 200 °C for 8 h. After being cooled down naturally to room temperature, final product was centrifuged and washed with ethanol and deionized water, followed by drying at 80 °C overnight.

2.3 Material Characterizations

X-ray diffraction (XRD, Rigaku D/Max-r B) was used to characterize the crystal phases. Field-emission scanning electron microscopy (FESEM, JSM-7610F) and transmission electron microscopy (TEM, JEOL JEM-F200) with the acceleration voltage of 200 kV were applied to

display the microstructures. Electrical conductivity was measured at room temperature by a ST-2258A digital four-point probe test system. Before the measurements, sample powders were compressed into a wafer with a thickness of 0.2 mm and a diameter of 13 mm by an oil pressure machine under a pressure of 30 MPa. Thickness of the nanosheets was measured by using an atomic force microscope (AFM) on a Bruker DI MultiMode-8 system. X-ray photoelectron spectroscopy (XPS, ESCALAB 250) was conducted to investigate surface chemical states. Raman spectra (LabRAM HR Evolution) with a 532-nm laser were used to further detect the material structures. Electron paramagnetic resonance (EPR, EMXnano) tests were performed at 300 K to confirm the defects. N_2 adsorption–desorption measurements (ASAP 2020) were implemented to detect the surface areas and pore sizes. Inductively coupled plasma spectrometer (ICP-OES, Agilent 5110) was used to determine element contents. The gas evolution rates of O_2, H_2O, and CO_2 were tested by in situ DEMS (i-DEMS 100). X-ray absorption fine structure (XAFS) spectra of Co K-edge were collected in transmission mode on a commercial Laboratory-Based XAFS spectrometer (Table XAFS-500A, Specreation Instruments Co., Ltd.). An X-ray tube was used to generate X-ray, and the voltage and current were set to 20 kV and 20 mA. The R250-mm Rowland circle was used to provide monochromatized X-ray beam.

2.4 Electrochemical Measurements

LOBs were assembled using CR 2032 coin-type cells with holes in their positive top covers for electrochemical tests. Electrolyte was composed of 1 M lithium bis(trifluoromethanesulfonyl)imide dissolved in trimethylene glycol dimethyl ether (LiTFSI/TEGDME). Active material, Ketjen black, and polytetrafluoroethylene (PTFE) polymer binder were mixed in 5 mL isopropanol solvent with a mass ratio of 4:4:2 to obtain the slurry, which was coated on the carbon paper on a heating base at 80 °C to fabricate the cathode. Lithium foil and glass fiber membrane were served as anode and separator, respectively. LOBs were assembled in an argon-filled glove box ($H_2O < 0.1$ ppm, $O_2 < 0.1$ ppm) and placed in a chamber purged with O_2 to investigate galvanostatic discharge/charge performance on a multichannel battery system (LAND CT 2001A). Cyclic voltammetry

(CV) testing at 0.15 mV s^{-1} within the potential range of 2.35–4.50 V (vs Li/Li$^+$) as well as electrochemical impedance spectroscopy (EIS) measurement with a limited frequency range of 10^5 to 10^{-2} Hz and a 10 mV oscillation amplitude was carried out on the electrochemical workstation (CHI760E).

In a pouch-type LOB, lithium foil (4×4 cm^2), 1T/2H-MCS-coated carbon cloth (4×4 cm^2), and 1 M LiTFSI/TEGDME-soaked glass fiber membrane (4.5×4.5 cm^2) were, respectively, used as the anode, the cathode, and the separator, which were encapsulated with perforated aluminum plastic film and sealed by a heat press sealer. The mass loading of 1T/2H-MCS is 16 mg for each cathode.

2.5 Theoretical Calculations

First-principles computations were employed by the Vienna Ab initio Simulation Package (VASP) based on DFT. The exchange–correlation energy of electrons was described using generalized gradient approximation (GGA) with the Perdew–Burke–Ernzerhof (PBE) parametrization. The core valence interaction was performed using the projector augmented wave (PAW) method. The cutoff energy was 450 eV and the k-point mesh was set to be $1 \times 1 \times 1$ for all slab calculations. The energy convergence criteria were set to 10^{-5} eV. A vacuum layer of 15 Å along the z-axis was applied to all slabs to avoid the periodic structural interactions. The maximum Hellmann–Feynman stress on each atom was set to be less than 0.02 eV Å^{-1}. All atoms were fully relaxed for the heterojunction structure optimizations, while the lower four layers of atoms were fixed for the structure optimization of all the catalytic intermediates.

3 Results and Discussion

3.1 Theoretical Prediction on Double Complementary Effect in 1T/2H-MoS$_2$@Co$_3$S$_4$

DFT calculations were conducted to investigate the phase transition mechanisms of MoS$_2$ after combined with Co$_3$S$_4$, and Fig. S1 displays the optimal structural models of the Co$_3$S$_4$, 2H-MoS$_2$, 2H-MoS$_2$@Co$_3$S$_4$, and 1T-MoS$_2$@Co$_3$S$_4$ heterostructures. In our previous research, DFT calculations of 2H-MoS$_2$ have been carried out by the same way as in this

work [36]. By Bader charge analysis, it is revealed that the electron transfer occurred from Co_3S_4 into $2H\text{-}MoS_2$ with an amount of 0.638 e, inducing phase transition from $2H\text{-}MoS_2$ to $1T\text{-}MoS_2$ (Figs. 1a and S2). Charge density difference and electron localization function (ELF) further prove the electron transfer from Co_3S_4 to $2H\text{-}MoS_2$ on heterogeneous interfaces, as shown in Fig. 1b. Therefore, the electron configuration of Mo $4d$ orbitals was rearranged. Based on crystal-field theory, Mo $4d$ orbitals of trigonal prismatically coordinated $2H\text{-}MoS_2$ cleavage into three energy levels: d_{z2} (a_1'), $d_{x2\text{-}y2}/d_{xy}$ (e'), and d_{xz}/d_{yz} (e'') orbitals. Two Mo d electrons could completely be filled to the lower-lying a_1' orbital, endowing the $2H\text{-}MoS_2$ semiconducting characteristic with high structural stability. In contrast, Mo $4d$ orbitals of octahedrally coordinated $1T\text{-}MoS_2$ cleavage into $d_{xy}/d_{xz}/d_{yz}$ (t_{2g}) and $d_{z2}/d_{x2\text{-}y2}$ (e_g) orbitals. Because of the incomplete occupation of the lower-lying t_{2g} orbitals, $1T\text{-}MoS_2$ shows metallic electronic property but poor structural stability [37].

To explain the interaction between Mo ions and the adjacent Co ions after combination, the partial electron transfer process from Co to Mo ions through the S ligand is illustrated in terms of their electronic configuration, as given in Figs. S3 and S4. As mentioned above, the a_1' orbital of Mo^{4+} with $4d^2$ trigonal prismatically coordinated geometry is fully occupied. In this condition, the major electronic interaction between the bridging S^{2-} and Mo^{4+} is $e^-\text{-}e^-$ repulsion. Similarly, trivalent Co ions present the valence electron configuration of $3d^6$ and exhibit low-spin octahedral geometry with fully occupied t_{2g} orbitals. After formation of heterostructures, the d electrons of Co $3d$ move to Mo $4d$. Due to the relative higher electronegativity of Mo ions, it thus can be claimed that the $e^-\text{-}e^-$ repulsion of Co–S bonds aided in intensifying the π-donation interaction between Mo^{4+} and S^{2-}, which trigger partial electron transfer from Co to Mo ions, accompanying the changes of coordination with surrounding S^{2-} [38]. As depicted in Fig. 1c, when $2H\text{-}MoS_2$ was combined with Co_3S_4, the extra electrons donated by Co_3S_4 firstly occupied the e' orbitals of $2H\text{-}MoS_2$, destabilizing the structure and inducing the Mo $4d$ orbital reorganization to generate MoS_2 transformation from 2H to 1T phase. As a result, the intrinsic electrical conductivity of MoS_2 was largely improved, which could serve as conductive phase for Co_3S_4. Total density of states (TDOS) around the Fermi level in Fig. 1d exhibits stronger metallic properties in $1T\text{-}MoS_2@Co_3S_4$. Particularly, the orbitals of Co $3d$, S $2p$,

and Mo $4d$ in Fig. 1e show substantial overlaps, implying strong electron interaction among them to accelerate electron transfer in the Co–S–Mo channels. Furthermore, after the combination of MoS_2 and Co_3S_4, the electron transferred from Co to Mo ions induced the downshift of the E_d of Co and the opposite trend of Mo (Fig. 1f), respectively, narrowing the energy differences between Co $3d$ and S $2p$ band centers and Mo $4d$ and S $2p$ band centers and thereby leading to the strong hybridization among Co, S, and Mo (Fig. 1g). The strong hybridization could improve the covalency Co–S–Mo bonds, which can directly facilitate the electron transport between Co ions and oxygen adsorbates via Co–S–Mo channels and activate the Co sites during the ORR process. Besides, the E_{ads} of LiO_2 on Co_3S_4 surfaces is extraordinarily strong, and it led to the high charge overpotentials, due to the fact that the decomposition of the discharge product needs to cross a higher energy barrier. However, when combined with $1T\text{-}MoS_2$, the E_{ads} of $1T\text{-}MoS_2@Co_3S_4$ could be reduced by modulated E_d of Co $3d$, which will be discussed in the following parts.

Based on the above analysis, Fig. 1h systematically demonstrates the synergistic effects of double complementary heterojunctions derived from charge donation from Co to Mo ions in 1T/2H-MCS. Specifically, according to theoretical calculations, $2H\text{-}MoS_2@Co_3S_4$ possesses suitable E_{ads} to efficiently adsorb and desorb the discharge product, but the overall electrical conductivity is poor due to the wide bandgap of $2H\text{-}MoS_2$. On the contrary, owing to the increasing DOS at the Fermi energy level, $1T\text{-}MoS_2@Co_3S_4$ exhibits excellent electrical conductivity via fast electron transport channels of Co–S–Mo bonds, while low antibonding orbital occupancy is unfavorable for adsorption of oxygen-containing intermediates, resulting from the large bandgap between E_d of Co and Fermi level. Therefore, 1T/2H-MCS containing complementary double heterojunctions is expected to enhance the catalytic activities of Co_3S_4.

3.2 Morphological and Structural Characterization

In a typical synthesis, ZIF-67 was applied as a template to obtain 1T/2H-MCS through a facile hydrothermal process (Fig. 2a), which could be divided into two steps. Under lower temperature, ZIF-67 was transformed into Co_3S_4 via a ligand exchange reaction between S_2^- and 2-methylimidazole, still
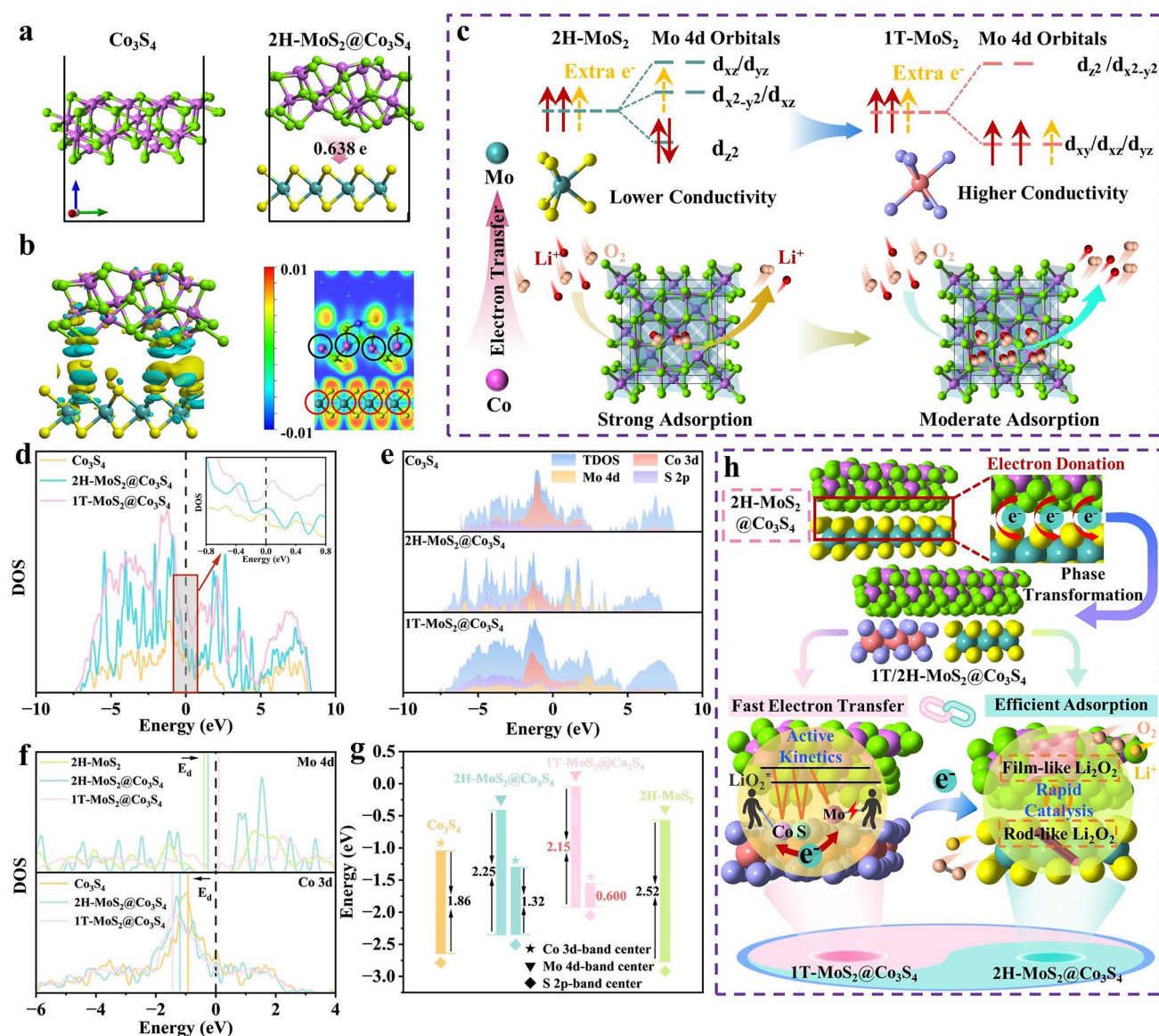
Fig. 1 **a** Bader charge transfer, **b** ELF, and charge density difference of 2H-MoS$_2$@Co$_3$S$_4$, in which charge accumulation and depletion are displayed by yellow and cyan, respectively. **c** Schematic diagram of proposed electron transfer processes between Co$_3$S$_4$ and 2H-MoS$_2$. **d** TDOS and **e** PDOS of different samples. **f, g** d-band and p-band centers of Co 3d, Mo 4d, and S 2p. **h** Schematic diagram of double heterojunction effects on 1T/2H-MCS for LOBs

maintaining rhombic dodecahedral shape. After higher temperature, disordered MoS$_2$ nanosheets grew on the surfaces of hollow Co$_3$S$_4$ polyhedrons to form 1T/2H-MCS. The digital photograph illustration of the synthesis path is given in Fig. S5.

To explore the crystalline structure and compositions of different samples, XRD, Raman, XPS, and EPR measurements were conducted. XRD analysis in Fig. 2b reveals that all characteristic peaks correspond to those of cubic Co$_3$S$_4$

(JCPDS 47-1738) and 2H-MoS$_2$ (JCPDS 75-1539), proving that 1T/2H-MCS were successfully synthesized. Figures S6a, S7a, and S8a exhibit XRD patterns of the precursor, Co$_3$S$_4$, and 2H-MoS$_2$, respectively. Raman data in Fig. S9 reveal that the peaks at 185 (A$_g$), 298 (F$_{2g}$), and 348 cm^{-1} (F$_{2g}$) are related to Co$_3$S$_4$, while the peaks at 375 (E1 2g) and 399 cm^{-1} (A$_g$) are associated with 2H-MoS$_2$ [39–41]. Four distinctive peaks at 140 (J$_1$), 193 (J$_2$), 278 (E$_{1g}$), and 333 cm^{-1} (J$_3$) can be also observed, originating from the
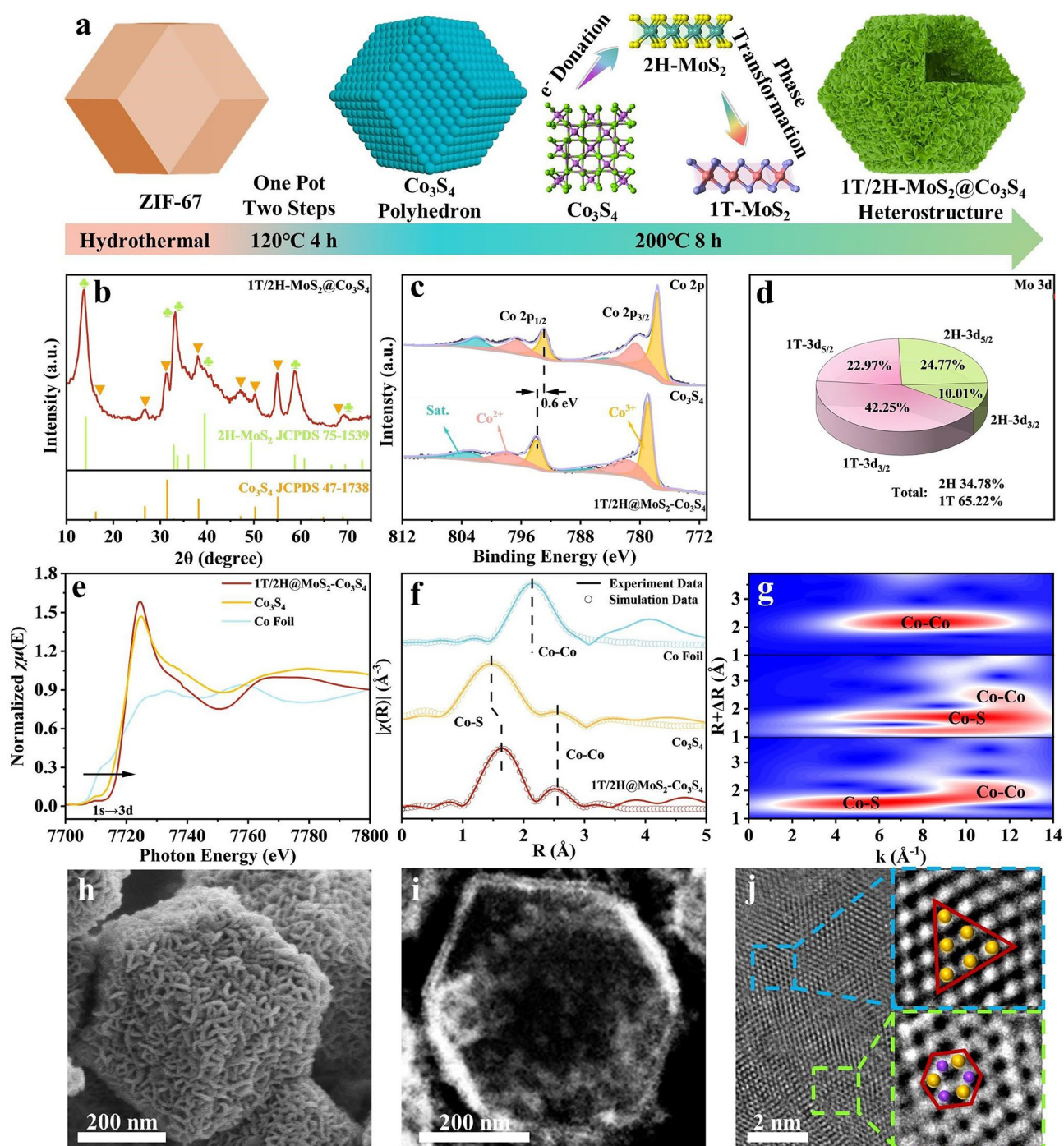
Fig. 2 **a** Schematic illustration of synthetic process for 1T/2H-MCS with the proposed phase transformation mechanism. **b** XRD pattern, **c** high-resolution Co 2*p* XPS spectra, **e** Co K-edge XANES spectra, **f** Fourier transform of Co K-edge EXAFS spectra, and **g** wavelet transform analysis of different samples. **d** 1T and 2H phase ratios, **h** FESEM image, **i** HAADF image, and **j** HRTEM image with enlarged results from corresponding selected areas of 1T/2H-MCS

phonon modes of 1T-MoS_2, and this demonstrates successful MoS_2 phase conversion from 2H to 1T after combination [42].

XPS survey spectra in Fig. S10 overview the elements existing on different samples. To provide a direct comparison, the Co 2*p* XPS spectra of Co_3S_4 and 1T/2H-MCS are

presented in Fig. 2e. Apparently, Co 2p XPS peak consists of two spin–orbit doublets, including Co 2$p_{3/2}$ and Co 2$p_{1/2}$ along with two satellites. Co^{3+} and Co^{2+} XPS peaks of Co$_3$S$_4$ position at 778.2/793.1 and 781.1/796.8 eV, whereas those of 1T/2H-MCS locate at 778.8/793.9 and 781.7/797.4 eV, respectively, indicating a binding energy red shift of 0.6 eV in 1T/2H-MCS relative to Co$_3$S$_4$. This XPS peak shift was attributed to changes in the oxidation state of the Co$_3$S$_4$ owing to MoS$_2$ presence. Detailed comparisons of Co^{2+}/Co^{3+} ratios in 1T/2H-MCS and Co$_3$S$_4$ are displayed in Fig. S11, showing the increased content of Co^{3+} from 48% to 65%. Co 2p XPS spectrum of 1T/2H-MCS displays higher oxidation states than that of Co$_3$S$_4$ owing to electron transfer at the interfaces of Co$_3$S$_4$ and 2H-MoS$_2$, which is also confirmed by Bader charge results [43]. Co 2p XPS spectrum of 1T/2H-MCS displays higher oxidation states than that of Co$_3$S$_4$ owing to electron transfer at the interfaces of Co$_3$S$_4$ and 2H-MoS$_2$ [43]. It is believed that high Mo electronegativity altered the Co electronic structure (σ*-orbital occupancy) by decreasing the Co electron density. Co σ*-orbital (e$_g$) occupancy is close to unity, which can boost the intrinsic ORR and OER activities toward oxygen species by promoted covalence of Co–O bonds [44, 45]. Figure S12 shows the corresponding high-resolution Mo 3d XPS spectra of 2H-MoS$_2$ and 1T/2H-MCS. Compared to Mo 3$d_{3/2}$ (232.3 eV) and Mo 3$d_{5/2}$ (229.2 eV) signals of pristine 2H phase, all the corresponding XPS peaks of 1T/2H-MCS blue-shift to lower binding energy at 231.9 and 228.8 eV. After fitting, the asymmetric signals can be divided into two peaks, and higher binding energy (labeled with green) and lower binding energy (labeled with pink), respectively, correspond to 2H and 1T MoS$_2$ phases, which is well consistent with Raman results [46, 47]. In terms of the deconvolution result of Mo 3d XPS spectra, the ratio of 1T phase is over 65% in the MoS$_2$ (Fig. 2d). It can be concluded the increased content of Co^{3+} could induce extra electron, occupying the e′ orbitals of 2H-MoS$_2$ to realize Mo 4d orbital reorganization and MoS$_2$ phase transformation from 2H to 1T. Accordingly, the high-resolution S 2p XPS spectra of 1T/2H-MCS in Fig. S13 are fitted into four peaks, which locate at 161.6/162.7 eV for 1T-MoS$_2$, 162.1/163.2 eV for 2H-MoS$_2$, and 163.7/164.9 eV for Co$_3$S$_4$. It is obvious that different shifts occurred for Co$_3$S$_4$ and 2H-MoS$_2$, demonstrating that the construction of the heterostructures enabled electron transfer from Co$_3$S$_4$ to 2H-MoS$_2$ through S-bridges. As shown in Fig. S14, EPR signal of 1T/2H-MCS (g = 2.003) corresponds to the unpaired Mo-S electrons on coordinatively unsaturated sulfur vacancy sites, which is stronger than those of Co$_3$S$_4$ and 2H-MoS$_2$ [48, 49]. Compared with 2H-MoS$_2$, the restriction growth of MoS$_2$ by Co$_3$S$_4$ triggered more unpaired electrons on (002) lattice planes, exposing more unsaturated sulfur edges on the surfaces of 1T/2H-MCS, and this is in accordance with TEM results.

Brunauer–Emmett–Teller (BET) measurements based on N$_2$ adsorption–desorption method were performed to investigate the specific surface areas and pore volumes. As shown in Fig. S15, the isotherms of 2H-MoS$_2$, Co$_3$S$_4$, and 1T/2H-MCS conform to the H3-type hysteresis loop, implying the presence of mesoporous structures in different samples. Typically, the isotherms of 1T/2H-MCS with inconspicuous adsorption platform demonstrate that this mesoporous structure is irregular. Specific surface area of 1T/2H-MCS (47.54 m^2 g^{-1}) is larger than those of Co$_3$S$_4$ (22.74 m^2 g^{-1}) and 2H-MoS$_2$ (11.34 m^2 g^{-1}). Compared with 2H-MoS$_2$, it is supposed that S^{2-} can quickly react with Co^{2+} to form hollow Co$_3$S$_4$ with high surface area at low temperature. The growth of small MoS$_2$ nanoflakes on the surfaces of Co$_3$S$_4$ at higher temperature could further enlarge the specific surface area. Moreover, the hollow Co$_3$S$_4$ structure endowed 1T/2H-MCS with a larger pore volume (0.21 cm^3 g^{-1}) than those of 2H-MoS$_2$ (0.071 cm^3 g^{-1}) and Co$_3$S$_4$ (0.153 cm^3 g^{-1}). It is believed that large specific surface area is beneficial to expose more active sites, promoting the formation and decomposition of discharge product. Moreover, more space could be enabled for fast mass transfer and enough discharge product storage. More importantly, the abundant mesopores in 1T/2H-MCS could contribute to effective electrolyte penetration, enlarging the electrolyte–catalyst interface area to accelerate oxygen catalysis reactions [50].

To further detect electronic structure and coordination information of Co species in 1T/2H-MCS, X-ray absorption spectroscopy (XAS) analysis was conducted. X-ray absorption near-edge spectra (XANES) of Co K-edge in Fig. 2e show that the Co K-edge of 1T/2H-MCS shifts to a higher energy position than those of Co foil and Co$_3$S$_4$, standing for an increasing Co chemical state in 1T/2H-MCS. The higher Co valence state in 1T/2H-MCS is consistent with the theoretical prediction and XPS results, suggesting that electron transferred from Co to Mo sites when combined with 2H-MoS$_2$ due to their electronegativity differences. Fourier

transform (FT) k^3-weighted EXAFS spectra of 1T/2H-MCS in Fig. 2f exhibit two apparent peaks located at 1.63 and 2.52 Å, which were ascribed to the Co–S and Co–Co contribution [51]. EXAFS spectra of Co K-edge were best fitted by including Co–S and Co–Co scattering path in fit model, as depicted in Table S1. Comparing 1T/2H-MCS with Co_3S_4, the first coordinative path of 1T/2H-MCS was expanded, which can be attributed to the asymmetric construction of Co–S–Mo after combining with $2H-MoS_2$. This coordination path can be better visualized in Fig. 2g by the maxima in the wavelet transform (WT) of the EXAFS, which is quite different compared to those of Co foil and Co_3S_4.

Morphology and structure information of these samples were captured by FESEM. As depicted in Fig. S6b, ZIF-67 exhibits a rhombic dodecahedral structure, and its surfaces are smooth without apparent wrinkles. Figure 2h presents the FESEM image of 1T/2H-MCS, which retained the typical dodecahedral rhombic shape of ZIF-67 and is decorated with random nanosheets with an average particle size of about 500 nm. For comparison, Figs. S7b and S8b show the FESEM images of Co_3S_4 and $2H-MoS_2$ samples, respectively, which display polyhedrons and large nanosheets with severe agglomeration. It is thus demonstrated that the ZIF-67 template can obviously restrict the layer-oriented growth of MoS_2. In addition, AFM was used to detect the flake thickness of 1T/2H-MCS. The result in Fig. S16a reveals that the MoS_2 nanoflakes formed by 6–7 monolayers, which is consisted with the following results of HRTEM images, and its corresponding 3D topography is offered in Fig. S16b. As shown in Figs. 2i and S17a, the high-angle annular dark-field (HAADF) and HRTEM images confirm that 1T/2H-MCS displays hollow structure containing Co_3S_4 nano-polyhedrons and outer MoS_2 nanosheets. Selected area electron diffraction (SAED) pattern agrees well with the crystal plane reflection of Co_3S_4 and $2H-MoS_2$, verifying the successful synthesis of $MoS_2@Co_3S_4$ heterostructures, as pictured in Fig. S18. From higher-magnification observation, the lattice fringe spacing of 0.284 nm corresponds to Co_3S_4 (311) planes, and there are some disordered regions generated by the lattice mismatch between Co_3S_4 and MoS_2 (Fig. S17b). Interestingly, after formation of MoS_2 and Co_3S_4 heterostructures, lattice structures of $1T-MoS_2$ in blue area and $2H-MoS_2$ in green area are observed simultaneously in Fig. 2j, further confirming the successful synthesis of 1T/2H-MCS. In Fig. S19, energy-dispersive X-ray (EDX) elemental mappings of 1T/2H-MCS manifest that Mo, Co, and S elements are evenly distributed throughout the entire architecture. Similarly, Figs. S20 and S21 display uniformly element distribution on Co_3S_4 and $2H-MoS_2$, respectively. Moreover, the element content results from EDX in Fig. S22 show that the molar ratio of Co_3S_4/MoS_2 in 1T/2H-MCS is 53.8/46.2, which is close to the inductively coupled plasma optical emission spectroscopy (ICP-OES) result (52.1/47.9), as demonstrated in Table S2.

3.3 Electrocatalytic Performance

Electrochemical tests were carried out to obtain insights into the ORR/OER catalytic activities of the prepared catalysts in LOBs. Figure 3a shows CV profiles of different cathodes within the voltage range of 2.35–4.50 V. It is found that 1T/2H-MCS cathode exhibits a higher onset potential for ORR (2.88 V) and a lower onset potential for OER (3.18 and 3.99 V), and its integral area is larger than those of other cathodes, implying better reaction kinetics and enhanced specific capacities [52]. During the cathodic scan, two small redox peaks during the ORR/OER processes demonstrate the stepwise formation/decomposition of intermediate LiO_2, indicating the fast ORR/OER kinetics of 1T/2H-MCS cathode. Figure 3b displays the initial galvanostatic discharge/charge performance for different cathodes at 100 mA g^{-1}. It is traced that 1T/2H-MCS cathode shows the highest discharge/charge specific capacities of 18,721/18,313 mAh g^{-1}, whereas those of the Co_3S_4, $2H-MoS_2$, and KB cathodes are 12,823/10,775, 8346/7744, and 5,195/3,394 mAh g^{-1}, respectively. Figure S23 shows the first discharge/recharge differential plots of 1T/2H-MCS cathode. The obvious peak corresponds to ORR voltage plateau at first discharging, while the two main peaks during OER process mean that charging reactions went through with two plateaus. It is apparent that 1T/2H-MCS cathode presents superior discharge/charge capacities with highest Coulombic efficiency and lowest overpotentials, agreeing well with CV results.

In Fig. 3c, the discharge/charge polarization of 1T/2H-MCS cathode gradually increased, and it still delivers impressive discharge specific capacities of 17,452, 12,804, 9,852, and 5,203 mAh g^{-1} at current densities of 200, 500, 800, and 1,000 mA g^{-1}, respectively, with corresponding Coulombic efficiencies of 97.2%, 91.3%, 86.7%, and 68.9%. In addition, the rate performance of different cathodes was also evaluated by terminal discharge/charge
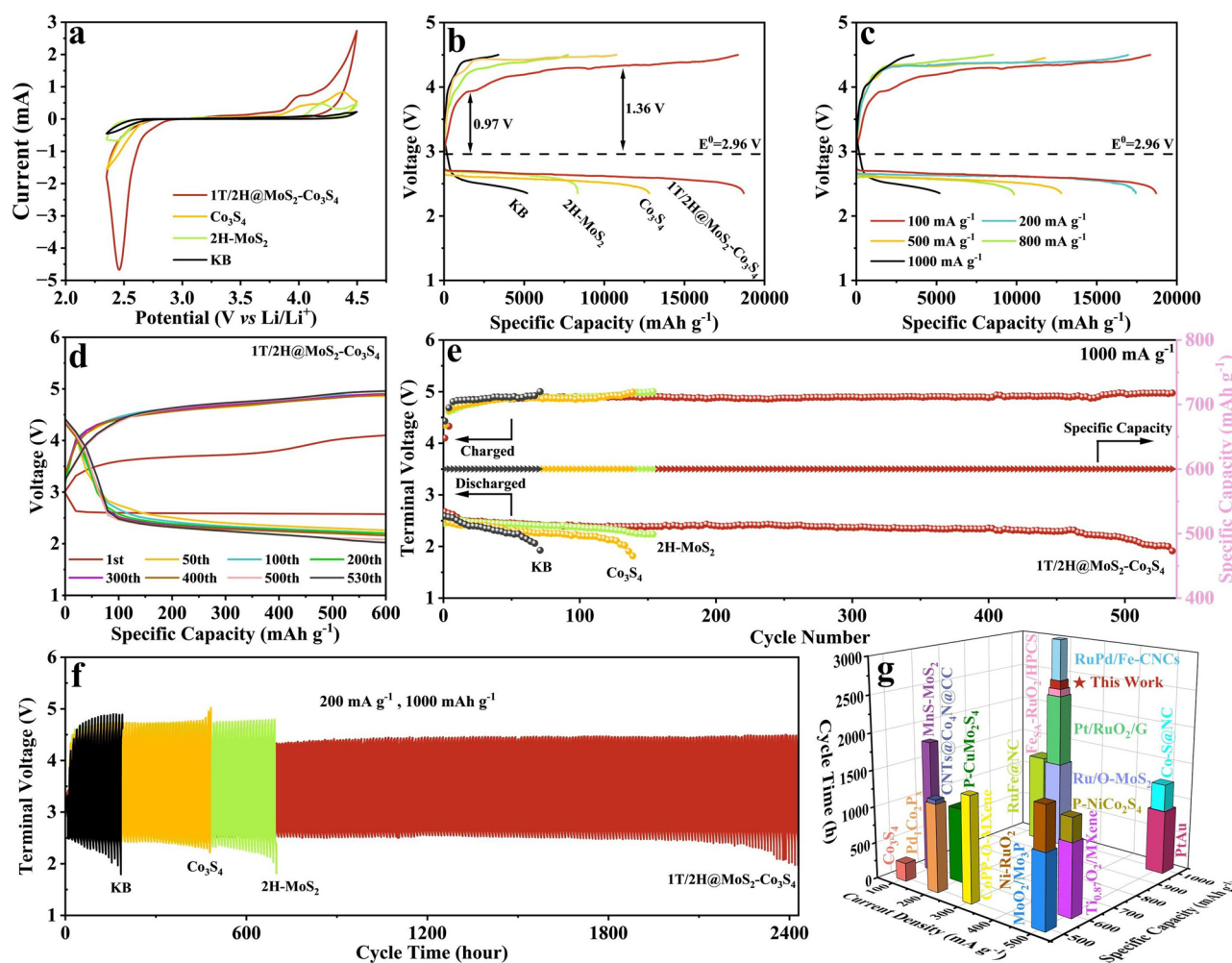
Fig. 3 **a** CV curves, **b** initial discharge/charge curves at 100 mA g^{-1}, **c** rate performance, as well as cycling duration **e** at 1000 mA g^{-1} under a specific capacity limit of 600 mAh g^{-1} with **d** selected charge–discharge profiles and **f** at 200 mA g^{-1} under a specific capacity limit of 1000 mAh g^{-1} of different cathodes. **g** Cycling stability comparison of 1T/2H-MCS cathode with representative and state-of-the-art cathodes containing Mo-, Co-, and noble metal-based compounds

voltage fluctuations at various current densities in Fig. S24. As current density increased (100, 200, 400, 800, and 1000 mA g^{-1}), the discharge and charge terminal voltages of the 1T/2H-MCS cathode only show slight variations of 0.20 and 0.24 V, respectively. After the current density was set to a primitive value, the discharge/charge terminal voltages exhibit highly reversible recovery, further manifesting the excellent rate reliability of 1T/2H-MCS cathode. The resistivity value of 1T/2H-MCS was measured as 82 Ω cm by using four-point probe techniques, which is much lower than that of 2H-MoS$_2$ (7.68×10^4 Ω cm) and Co$_3$S$_4$

(1.86×10^3 Ω cm) [53, 54]. It is believed that by the formation of 1T-MoS$_2$ with the fast charge transfer channels of Co–S–Mo at the interfaces, the electronic conductivity of the 1T/2H-MCS cathode could dramatically increase, which enabled fast charge transfer and electrochemical performance improvement at high current densities.

Long-term cycling performance of different cathodes in LOBs was investigated. Figure S25 illustrates that 1T/2H-MCS cathode can stably work for 344 cycles, whereas the 2H-MoS$_2$, Co$_3$S$_4$, and KB cathodes gradually decayed after 176, 149, and 60 cycles with a cutoff specific capacity of

600 mAh g^{-1} at 500 mA g^{-1}. It can also be seen in Fig. 3d–f that 1T/2H-MCS cathodes display an impressive cycle duration of 535 cycles at a high current density of 1000 mA g^{-1} and an ultralong cycle life of 2420 h with a fixed specific capacity of 1,000 mAh g^{-1}. Figure 3g and Table S3 show battery performance comparison of the representative and state-of-the-art cathodes containing Mo-, Co-, and noble metal-based compounds with the result in this work. It is worth noting that the cycling stability of 1T/2H-MCS cathode exhibits comparable performance and even outperforms some of noble metal-based counterparts. These improved electrocatalytic activities are attributed to the phase transformation of MoS$_2$ from 2H to 1T by electron transfer, delivering a higher electrical conductivity, while the 2H phase can act as a stabilizer to keep the 1T phase structure stable during cycling. Meanwhile, the Co ions in Co$_3$S$_4$ with modulated e$_g$ orbital occupancy after the electron transfer could promote the ORR/OER kinetics. In addition, after combining with 2H-MoS$_2$, the E$_d$ of Co slightly moved away from the Fermi level, which optimized the adsorption ability for the discharge product and further improved the battery performance.

3.4 Practical Application in Pouch-Type Batteries

It is demonstrated in Fig. 4a that the flexible pouch-type LOB was constructed. As shown in Fig. 4b, it can obtain discharge/charge specific capacities of 16,875/16252 mAh g^{-1} and a high capacity retention of 96%, indicating excellent ORR/OER kinetics of 1T/2H-MCS cathode. Impressively, it could be continuously operated for 375 cycles with a limited specific capacity of 1 mAh cm^{-2} at 0.5 mA cm^{-2}, revealing a considerable cycling stability, as offered in Fig. 4c. To clearly demonstrate battery electrochemical stability, the open-circuit voltages of the LOBs with 1T/2H-MCS cathodes were tested under different bending angles (Fig. 4d), displaying almost no change even battery corner was cut and was under 180° bent at the same time. It is also demonstrated that two pouch-type LOBs could be connected in series with the open-circuit voltage of 5.84 V (Fig. S26). As illustrated in Fig. 4e, the smartphone can be successfully charged using the above batteries, which can also charge a smartwatch with its power increasing from 73% to 84% in 21 min (Fig. 4f). It is suggested that high energy density and durability of the pouch-type LOBs with 1T/2H-MCS cathodes are highly beneficial for supporting next-generation electronic devices.

3.5 Electrochemical Analysis

To investigate the morphology and structural evolution of discharge product on the different cathodes, ex situ XRD, ex situ FESEM, ex situ XPS, and in situ differential electrochemical mass spectrometry (DEMS) analysis were applied to characterize the reaction processes at different states during discharge/charge processes. Ex situ XRD results show that the main discharge product on 1T/2H-MCS cathode is Li$_2$O$_2$ with poor crystallinity (Fig. S27), which disappeared after recharging. Even after 100 cycles, Li$_2$O$_2$ was nearly decomposed to expose catalyst surfaces again, demonstrating negligible accumulation of the discharge product and efficient catalysis activities of 1T/2H-MCS. Similar conclusion can also be drawn by Raman spectra in Fig. S28, and it is demonstrated that the side reactions were significantly inhibited, and the Li$_2$O$_2$ was fully decomposed [55]. Interestingly, the peaks of 1T-MoS$_2$ were detected at different stages during cycling, indicating improved stability. According to previous studied, the existence of 2H-MoS$_2$ can contribute to stabilizing 1T-MoS$_2$, avoiding restacking as well as transformation into the 2H phase [35]. Furthermore, the morphology evolution of the 1T/2H-MCS, Co$_3$S$_4$, and 2H-MoS$_2$ cathodes at different stages during 1st discharging/charging was observed from ex situ FESEM images. It is apparent that the dense film-like discharge product was adhered to the surfaces of Co$_3$S$_4$ cathodes, as shown in Fig. 5a, b, leading to cathode passivation with limited specific capacities [56]. However, since the E$_{ads}$ of 2H-MoS$_2$ for reaction intermediates is weak, the discharge product tends to form the rod-like Li$_2$O$_2$ through a solution-mediated pathway. It is noted that the poor catalytic activities of 2H-MoS$_2$ as well as limited contact between it and the rod-like Li$_2$O$_2$ result in higher overpotentials and unsatisfactory cycle performance due to incomplete decomposition of discharge product, as can be seen in Fig. S29a, b. Interestingly, the film- and rod-like Li$_2$O$_2$ generated simultaneously on the surfaces of 1T/2H-MCS cathode, which were caused by moderate adsorption energy of active sites for reaction intermediates. Actually, the discharge product on 1T/2H-MCS cathode coexisted in two forms, allowing for more accommodation of discharge product and a significant increase in discharge specific
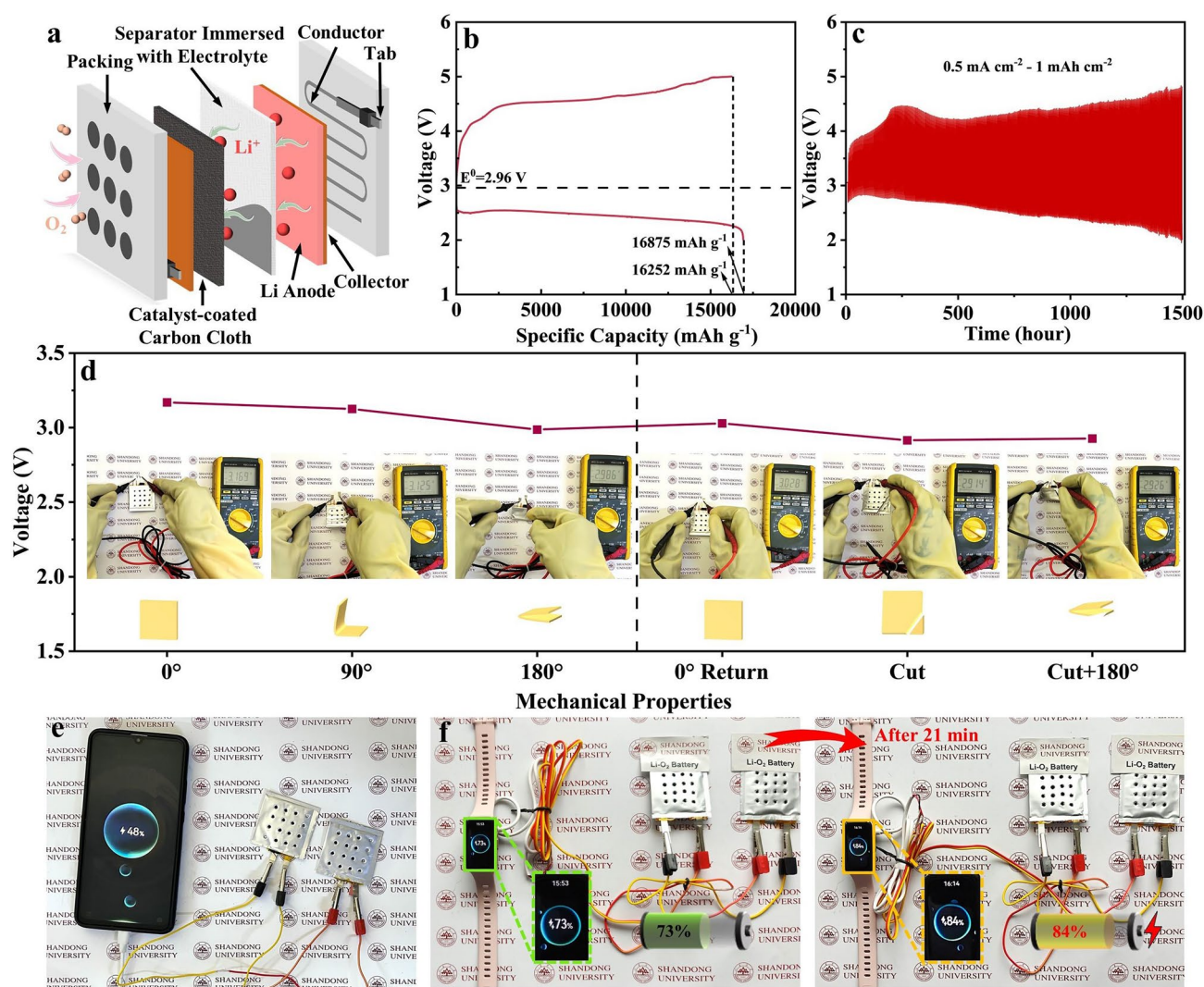
Fig. 4 **a** Schematic illustration of the configuration, **b** initial discharge/charge performance, **c** cycling duration at 600 mA g^{-1} under a specific capacity limit of 1800 mAh g^{-1}, **d** open-circuit voltages of different deformation states, and **e, f** practical applications of pouch-type LOBs

capacity. Figure S30 displays the morphology of the discharge product for 1T/2H-MCS cathode after discharging to 1,000 mAh g^{-1}. It is clear that the loose film-like and fine rod-like discharge product first formed, and it then grew into a uniform film and thick rod morphology with discharge capacity increase, which revealed the co-growth mechanism of the film- and rod-like Li$_2$O$_2$ on 1T/2H-MCS cathode. As shown in Fig. S31a, after 100th discharging, the film- and rod-like Li$_2$O$_2$ still could be observed on the surfaces of 1T/2H-MCS cathode, which is similar with that at 1st discharging, indicating the stability of the solution and surface dual reaction pathways on 1T/2H-MCS cathodes. Furthermore, the 1T/2H-MCS cathode could still maintain

the original morphology after 100th recharging (Fig. S31b). In contrast, as shown in Figs. 5c, f and S29c, a large number of residues still remained on the surfaces of Co$_3$S$_4$ and 2H-MoS$_2$ cathodes. They not only covered the active sites on the cathode surfaces, but also blocked the Li$^+$/O$_2$ transfer channels, thus ultimately leading to battery performance fails [57].

EIS plots of different cathodes were used to identify the intrinsic kinetics characteristic at different stages. As shown in Fig. S32, 1T/2H-MCS cathode presents smaller semicircles, and this implies a superior electrical conductivity for the phase transformation of MoS$_2$ from 2H to 1T, which is well consistent with TDOS results in Fig. 1d.
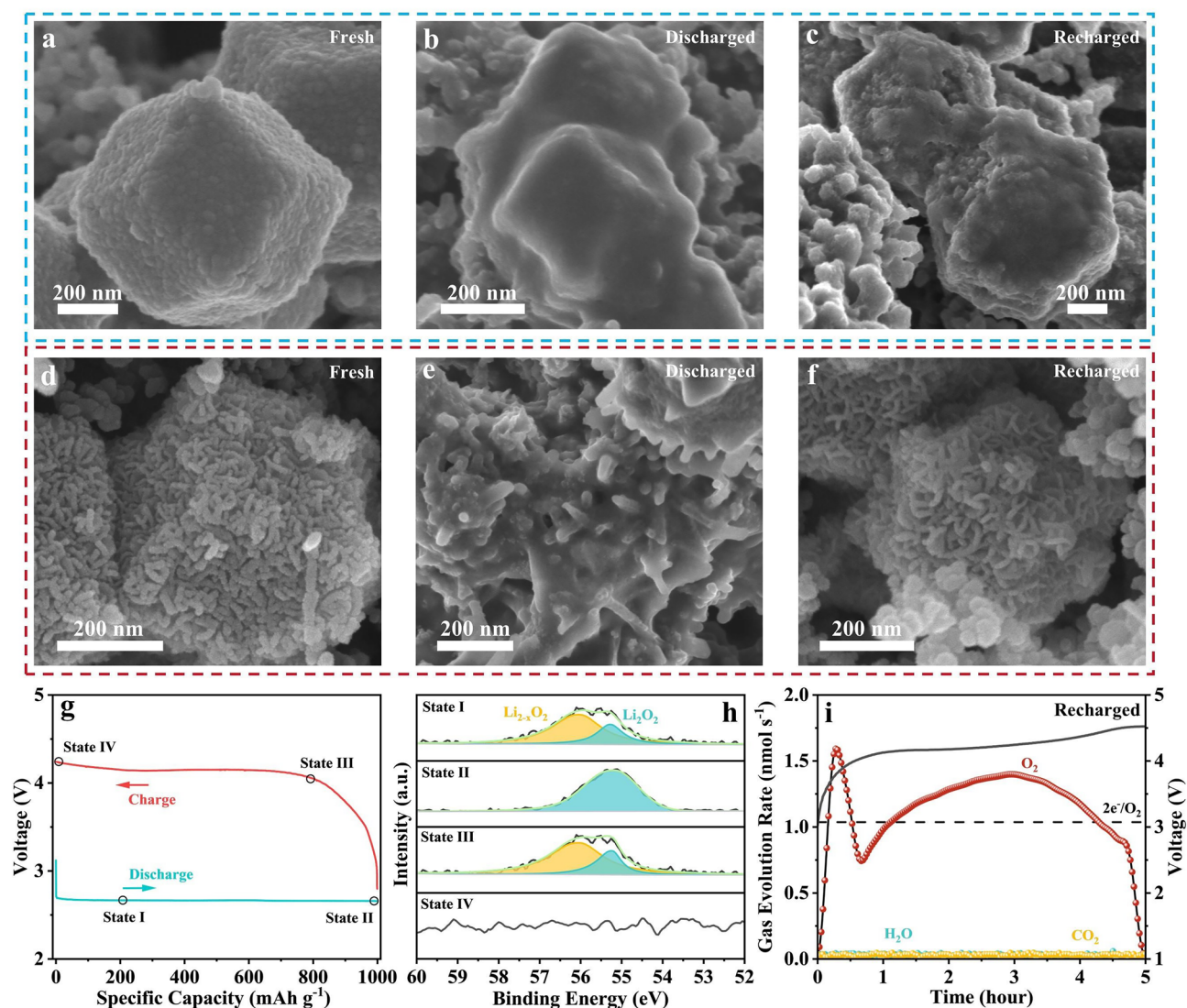
Fig. 5 FESEM images of **a–c** Co$_3$S$_4$ and **d–f** 1T/2H-MCS cathodes at different states. **g** Initial discharge/charge curves at 200 mA g^{-1} under a cutoff specific capacity of 1000 mAh g^{-1}, **h** high-resolution Li 1s XPS spectra at different states, and **i** in situ DEMS profiles with the charge curve at 200 mA g^{-1} of 1T/2H-MCS cathodes

After discharging, it is clear that charge transfer resistance (R_{ct}) increased from 21.9 to 85 Ω, which is still lower than those of Co$_3$S$_4$ and 2H-MoS$_2$ cathodes due to the unique morphology evolution of the discharge product on cathode surfaces, promoting the charge transfer on 1T/2H-MCS cathodes. In addition, after 1st and 100th recharging, their R_{ct} shows insignificant changes compared to that of the fresh cathode. In contrast, a remarkable R_{ct} increment of Co$_3$S$_4$ and 2H-MoS$_2$ cathodes can be detected after 1st discharging and charging, indicating that the dense film- and rod-like Li$_2$O$_2$/catalyst interfaces increased the charge

transfer resistance and lead to obvious reaction polarization [58]. It is thus concluded that the 1T/2H-MCS cathodes show excellent electrical conductivity and moderate adsorption ability toward discharge product during cycling.

To further explore the chemical conditions of discharge product and reaction mechanisms in discharge/charge processes, ex situ high-resolution Li 1s XPS spectra of 1T/2H-MCS cathodes with selected pivotal states (Fig. 5g, h) at 200 mA g^{-1} were studied. It is worth noting that the primarily discharge product on 1T/2H-MCS cathode

is $Li_{2-x}O_2$ (a low crystalline mixture of Li_2O_2 and LiO_2) with the peak at 56.1 eV, and it transformed to Li_2O_2 during subsequent discharging, which is similar on Co_3S_4 and 2H-MoS_2 cathodes [59]. However, signals of Li_2CO_3 appeared at 55.6 eV for Co_3S_4 and 2H-MoS_2 cathodes. This indicates that side reactions occurred during the discharge process, and Li_2CO_3 remained when recharged to a limited specific capacity of 500 mAh g^{-1}, which were accumulated during cycling and degraded battery performance, as evidenced in Figs. S33 and S34. Subsequently, in situ DEMS was conducted to determine the evolution of gas species in discharge/charge reactions. To calculate the electron-to-O_2 (e$^-$/O_2) ratio, the intrinsic micro-electrochemical processes were evaluated using the following equations, as determined by the amount of e$^-$ passed during charging and the integrating curves of the O_2 consumption rate:

$$Q = I \times t \qquad (1)$$

$$v(e^-) = Q \times e^- \qquad (2)$$

$$v(O_2) = GasEvol.\ Rate/60 \times N_A \qquad (3)$$

In situ DEMS results of different cathodes were obtained at 500 mA g^{-1} during charging, as provided in Figs. 5i, S35b, and S36b. It is clear that the e$^-$/O_2 ratio for 1T/2H-MCS was found to be close to 1.92, indicating the simultaneous decomposition of Li_2O_2 (2e$^-$/O_2) and LiO_2 (e$^-$/O_2). In contrast, the values of Co_3S_4 and 2H-MoS_2 are, respectively, 2.88 and 2.58, much higher than that for 1T/2H-MCS. This indicates incomplete decomposition of the discharge product and severe parasitic reactions, which is consistent with ex situ FESEM and ex situ XPS results [60]. Typically, O_2 evolution plots for each cathode present typical "M" shape during charging, demonstrating stepwise decomposition of Li_2O_2, and an increased maximum O_2 gas precipitation was presented at lower potential for 1T/2H-MCS cathode, which could be attributed to enhanced OER catalytic abilities [61]. Furthermore, it is apparent that an amount of CO_2 gas evolved at the end of charging state for both Co_3S_4 and 2H-MoS_2 cathodes, providing strong evidence that severe parasitic reactions occurred in recharge process to pose poor reversible specific capacity. During discharging, all curves are similar, and e$^-$/O_2 ratios are all close to the 2 for desired O_2

reduction to Li_2O_2, as listed in Figs. S35a, S36a, and S37. These results demonstrate that the 1T/2H-MCS cathode could deliver moderate adsorption ability and significantly inhibit side reactions, thus exhibiting superior electrocatalytic activities for ORR/OER processes in LOBs.

To further elucidate the effect of double heterojunction effects in 1T/2H-MCS, samples of MoS_2 mixed Co_3S_4 in the ratio of 1:1 (MoS_2 Mixed Co_3S_4) were prepared. Since the DOS distributions of Co 3d, S 2p, and Mo 4d are mismatched, and it is hard to form chemical bonds between Co_3S_4 and MoS_2 through simple mixing. In Fig. S38a, the ratio of Co^{2+}/Co^{3+} in MoS_2 Mixed Co_3S_4 is 46/54, which is similar to that in pure Co_3S_4, proving the limited charge donation from Co to Mo ions, and only 2H-MoS_2 is present in MoS_2 Mixed Co_3S_4, as shown in Fig. S38b. Consequently, MoS_2 Mixed Co_3S_4 cathode shows unsatisfactory initial discharge/charge capacities of 11,037/8,400 mAh g^{-1} with poor Coulombic efficiency, as depicted in Fig. S39a. As for rate performance, discharge/charge terminal voltages decreased/increased obviously as the variation of current density (Fig. S39b). Furthermore, the EIS plots of MoS_2 Mixed Co_3S_4 cathodes were collected at different stages in Fig. S40. The MoS_2 Mixed Co_3S_4 cathode still displays a large R_{ct} of 169 Ω after recharging, indicating sluggish reaction kinetics during OER process. The above results confirm that the double heterojunction effects in 1T/2H-MCS play a critical role in enhancing electrochemical performance.

3.6 Proposed Mechanisms by DFT Calculations

To further clarify the catalytic mechanisms, DFT calculations were carried out to simulate the formation/decomposition of the discharge product on the cathode catalysts. Figure S41 shows different optimized structures after adsorbing different oxygen species (LiO_2, Li_2O_4, Li_3O_4, and Li_4O_4), and corresponding charge density difference plots and Bader charge transfer of different oxygen species on the surfaces of Co_3S_4, 2H-MoS_2, 2H-MoS_2@Co_3S_4, and 1T-MoS_2@Co_3S_4 are shown in Figs. 6a and S42-S45. In those models, the yellow and blue areas denote the gained electrons and lost electrons, respectively. As for the adsorption models of 2H-MoS_2, 2H-MoS_2@Co_3S_4, and 1T-MoS_2@Co_3S_4, the charge could transfer from oxygen-containing intermediates to catalysts, with more charge transferred to the active sites on 2H-MoS_2@Co_3S_4, efficiently promoting desorption of LiO_2 and thus greatly enhancing catalyst reaction kinetics

[62]. While for the Co_3S_4, the charge transferred to oxygen-containing intermediates, which is unfavorable for the catalytic conversion and lead to increased overpotentials [63].

It is noted that covalency of metal–oxygen bonds serves as another essential descriptor for the electrocatalytic activities during the reaction processes, as it is closely linked to the interfacial electron transfer kinetics involved in oxygen redox reactions [64]. Typically, a modest increased covalency of metal–oxygen bonds tends to mitigate the electron transfer energy barrier. It can be found in Fig. 6b that PDOS shows a middle overlap degree between Co 3*d*- and O 2*p*-orbitals near the Fermi level in 2H-MoS$_2$@Co$_3$S$_4$, compared to those in Co$_3$S$_4$

and 1T-MoS$_2$@Co$_3$S$_4$, which demonstrates the moderate adsorption of LiO$_2$ on the 2H-MoS$_2$@Co$_3$S$_4$. Simultaneously, an increased energy gap between the Co 3*d* and O 2*p* band centers can be observed in Fig. 6b. The expanding of the energy difference between the Co 3d and O 2*p* band centers also manifests the weak hybridization between the Co 3*d* and O 2*p*, undermining the covalency of Co–O bonds. According to Sabatier principle [65], the strong covalency of Co–O bonds could result in the deactivation of active sites to increase the overpotentials. On the contrary, weak covalency of Co–O bonds could lead to unrestricted growth of Li$_2$O$_2$ and thus limit the contact between Li$_2$O$_2$ and cathode surfaces, deteriorating LOB

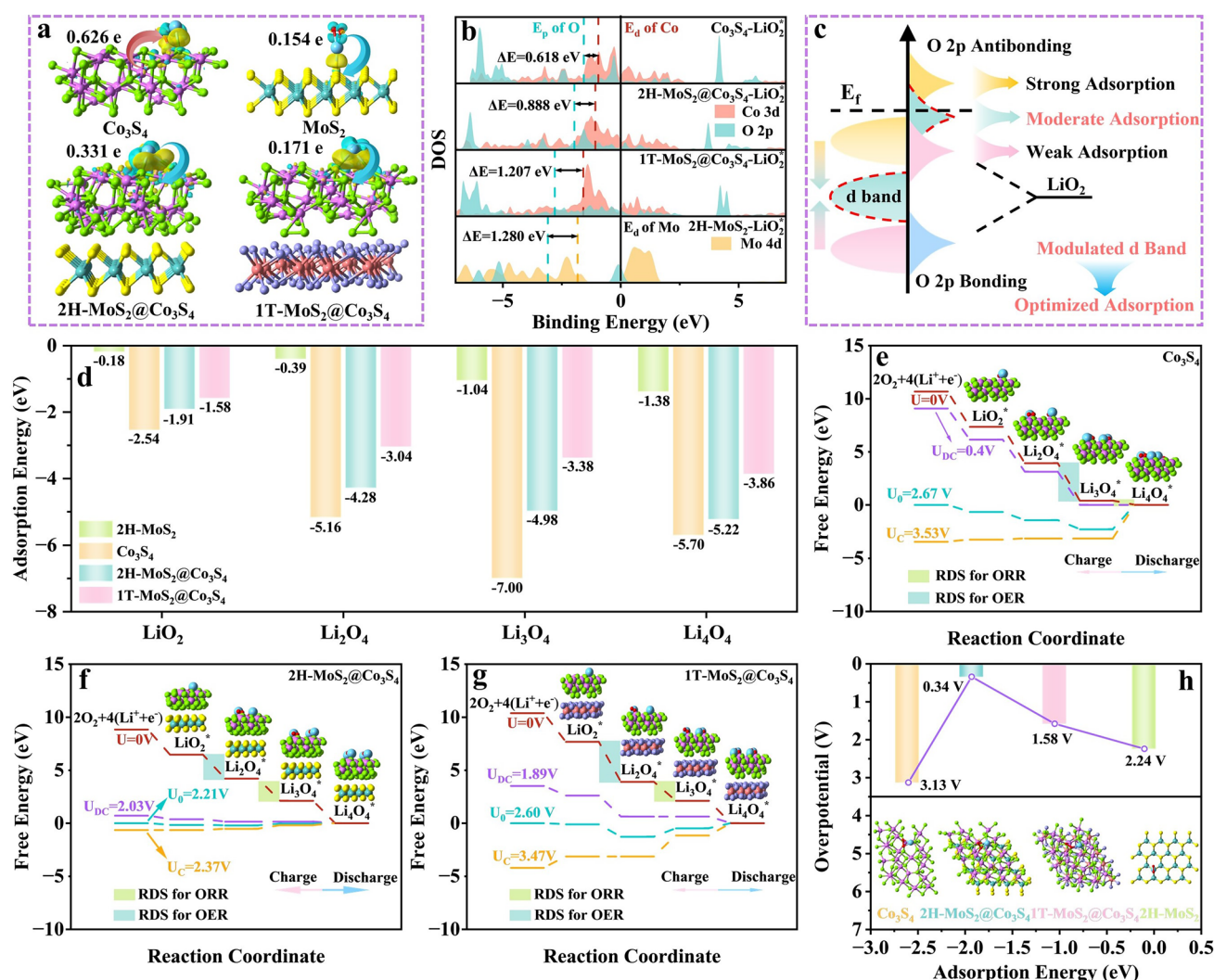**Fig. 6** **a** Charge density differences with Bader charge transfer, **b** d-band and p-band centers of Co 3*d* and S 2*p* of different catalysts. **c** Schematic illustration of d-p orbital hybridization for 1T/2H-MCS. **d** Adsorption energy and the relationship between adsorption energy and overpotentials, **e–g** Calculated energy diagrams, and **h** relationship between adsorption energies and overpotentials of different catalysts

performance. Besides, the overloaded adsorbed discharge product was prone to fall off the cathode, inducing discharge product loss at deep discharge state. Thus, it is concluded that $2H-MoS_2@Co_3S_4$ with moderate d-p orbital hybridization of LiO_2 could exhibit abundant adsorption sites and superior OER/ORR kinetics. Furthermore, the $2H-MoS_2@Co_3S_4$ possesses optimized E_d value of Co with moderate Co–O antibonding orbital occupancy, which contributed to the optimal bonding interaction between Co sites and oxygen-containing intermediates for suitable oxygen adsorption and boosted electrocatalysis (Fig. 6c). Distinct differences between four models before and after adsorption of LiO_2 can be traced in Fig. S46, indicating effective adsorption of $2H-MoS_2@Co_3S_4$ due to the optimized d-p orbital hybridization with LiO_2. Detailed adsorption energy of the four catalysts for the reaction intermediates is clearly observed in Fig. 6d. It is widely accepted that the intrinsic adsorption energy (ΔE_{ads}) of LiO_2 intermediate on catalyst surfaces is a crucial factor in regulating the nucleation and growth mechanisms of Li_2O_2 during discharge process [66, 67]. Strong affinity of LiO_2 on Co sites of Co_3S_4 promoted the accumulation of LiO_2 with high local concentration and hence resulted in generation of dense film-like Li_2O_2 through surface growth pathway, which is unfavorable for mass diffusion and thus suppressed the subsequent Li_2O_2 formation. As for $1T-MoS_2@Co_3S_4$ and $2H-MoS_2$, due to their poor adsorption capability of LiO_2, LiO_2 tended to be dissolved in electrolyte and disproportionate to form Li_2O_2 nanorods. The oxidation of Li_2O_2 nanorods brought about high overpotentials because of poor interfacial contact between nanorods and catalytic active surfaces.

The TDOS data for Co_3S_4, $1T-MoS_2@Co_3S_4$, $2H-MoS_2@Co_3S_4$, and $2H-MoS_2$ before and after adsorptions of different reaction product are given in Fig. S47. TDOS result of $2H-MoS_2@Co_3S_4$ around the Fermi energy level exhibits a significant increase, and this represents enhanced electrical conductivity upon loading of the intermediates, which due to the optimized interaction between $2H-MoS_2@Co_3S_4$ and discharge product. However, opposite change for Co_3S_4 appears, suggesting that the insulated discharged product decayed the electrical conductivity of Co_3S_4 due to the strong adsorption ability. Phase diagram of the cathode reactions provides in-depth insights into the process of discharge product evolution, as depicted in Fig. S48. As for $2H-MoS_2@Co_3S_4$, LiO_2 with a low ΔG formed spontaneously in the interval

of 2.17–2.37 V. When the discharge voltage is below 2.17 V (the cross point between Li_2O_4 and Li_3O_4 line), Li_2O_2 with a thermodynamic advantage began nucleation. As the voltage dropped to 2.05 V, steady Li_4O_4 clusters generated. These results demonstrate that $Li_{2-x}O_2$ easily grew on $2H-MoS_2@Co_3S_4$ surfaces, which could change the nucleation route of Co_3S_4 after the formation of 1T/2H-MCS. To understand the configuration of oxygen-containing intermediates during the discharging process, O–O bond lengths, O–Li–O bond angles, and adsorption distances of oxygen-containing intermediates of four catalysts are compared in Figs. S49–S52. Due to the strongest/weakest d-p orbital hybridization of Co_3S_4 and MoS_2, different oxygen-containing intermediates are all closest/farthest to/from the catalyst surfaces, which is in accordance with adsorption energy results. Furthermore, the bond lengths of O–O in oxygen-containing intermediates on $2H–MoS_2@Co_3S_4$ are in the middle of those on $1T-MoS_2@Co_3S_4$ and Co_3S_4, and the O–Li–O bond angles on $2H-MoS_2@Co_3S_4$ are twisted to a larger angle (the standard value is 45.6°), leading to a facile cleavage of the O–O bonds. Accordingly, heterojunctions of $2H-MoS_2@Co_3S_4$ could play an effective role in optimizing the adsorption of oxygen species and accelerating the O–O bond breakages.

Free energy calculations were used to determine the energy required for each reaction stage. OER/ORR overpotentials are defined as $\eta_{OER} = U_C-U_0/\eta_{ORR} = U_0-U_{DC}$. U_C, U_{DC}, and U_0, respectively, denote minimum charge, maximum discharge, and equilibrium potentials. $2H-MoS_2@Co_3S_4$ cathode exhibits the lowest η_{OER}/η_{ORR} (0.16/0.18 V) among those of Co_3S_4 (0.86/2.27 V), $1T-MoS_2@Co_3S_4$ (1.17/0.81 V), and MoS_2 (0.70/1.54 V) in Fig. 6f, revealing significantly promoted electrocatalytic activities of the $2H-MoS_2@Co_3S_4$ toward oxygen redox reactions in LOBs due to the moderate d-p orbital hybridization with oxygen-containing intermediates (Fig. 6e, g). Based on the above results, volcano-like relationship between binding energy of oxygen-containing intermediates with different catalysts and overpotentials can be established in Fig. 6h. Optimal binding energy of oxygen-containing intermediates on $2H-MoS_2@Co_3S_4$ is of great essence to improve its electrocatalytic activities, which is in conformity with the Sabatier principle. Particularly, owing to weak adsorption of oxygen-containing intermediates, the coverages of reactive oxygen species on $1T-MoS_2@Co_3S_4$ and $2H-MoS_2$ are relatively low and thus contributed less to oxygen electrocatalytic activities and electron transfer. On the contrary, excessive adsorption
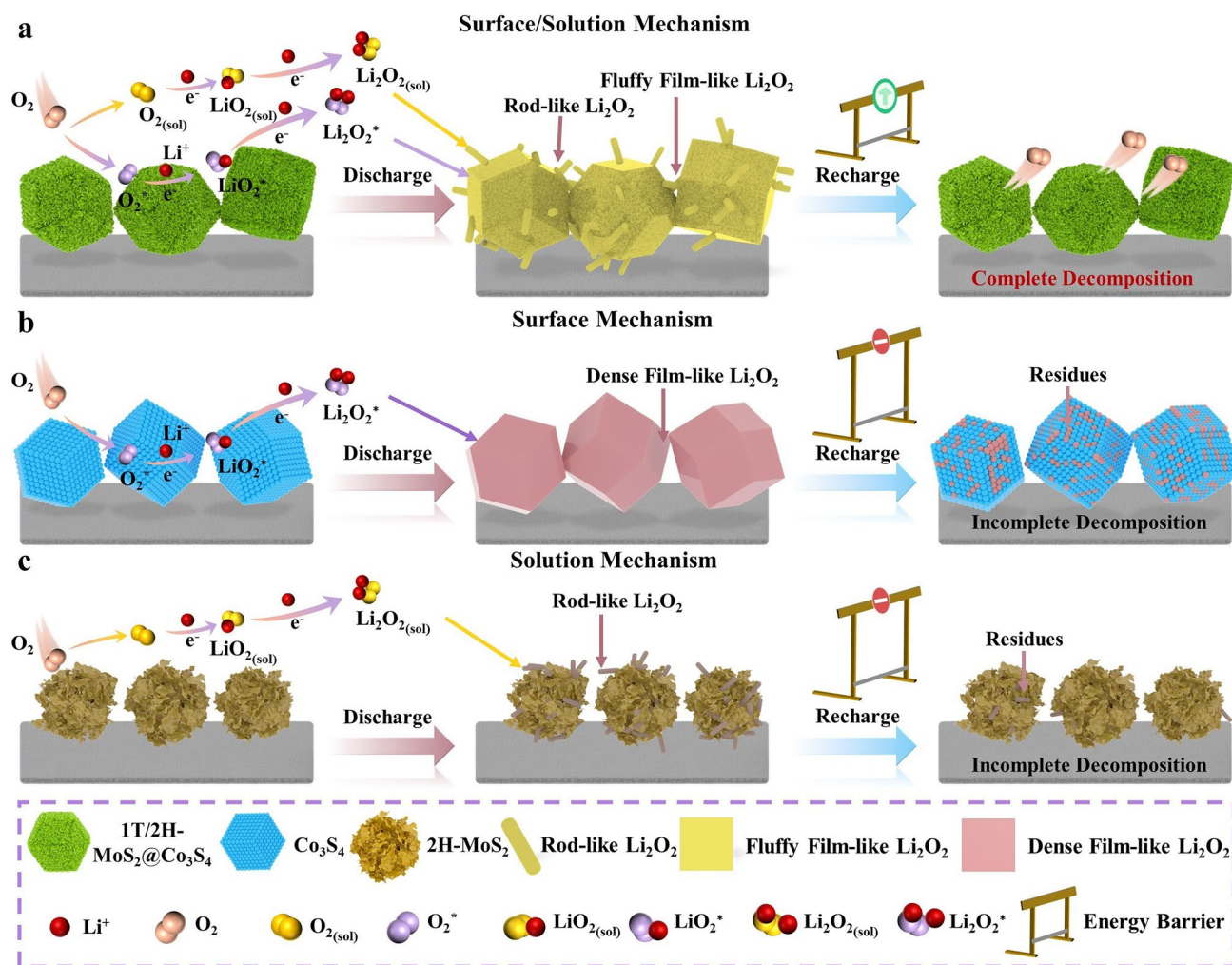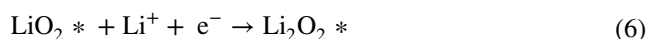
Scheme 1 Proposed electrocatalytic mechanisms of **a** 1T/2H-MCS, **b** Co$_3$S$_4$, and **c** 2H-MoS$_2$ cathodes during ORR/OER processes

of reactive oxygen species on Co$_3$S$_4$ poisoned active sites and thus impeded reaction kinetics. Therefore, an appropriate binding energy of oxygen species on 2H-MoS$_2$@Co$_3$S$_4$ could not only increase reactive oxygen species coverage, but also prevent poisoning effect caused by blockage of active sites, thereby beneficial for remarkable electrochemical performance of 1T/2H-MCS cathodes.

Rational formation and decomposition pathways of the discharge product on different cathodes are elucidated in Scheme 1. It is proposed that intermediate product LiO$_2$ first generated via a one-electron reduction reaction on the cathode surfaces (Eq. (4)). For the 2H-MoS$_2$ cathode, due to extremely weak binding energy for LiO$_2$, the intermediate was then dissolved in the electrolyte, defined as LiO$_{2(sol)}$, which was further converted to the rod-like Li$_2$O$_2$ via solution growth pathway (Fig. S29b and Eq. (5)). During charging process, low catalytic activities, poor electrical conductivity, and limited contact with rod-like Li$_2$O$_2$ resulted in extremely low discharge specific capacities and unsatisfactory cycle performance of 2H-MoS$_2$ cathodes. Inversely, the strong adsorption energy of LiO$_2$* on the Co$_3$S$_4$ surfaces promoted the formation of dense film-like Li$_2$O$_2$ through surface growth pathway (Fig. 5b and Eq. (6)). They were closely adhered to the cathode surfaces to slow down the kinetic diffusion of electrons/ions on the cathode catalyst, which lowered the activation and led to high interfacial polarization. Fortunately, owing to moderate adsorption energy of 1T/2H-MCS for LiO$_2$*, Li$_2$O$_2$ were grown on 1T/2H-MCS cathode via solution and surface dual pathways, forming two kinds of different morphologies (Fig. 5e).

Enhanced catalytic activity of 1T/2H-MCS via the synergistic effects of double complementary heterojunctions from 1T-MoS$_2$@Co$_3$S$_4$ and 2H-MoS$_2$@Co$_3$S$_4$ changed the affinity between the catalyst surfaces and the reaction intermediates to affect LiO$_2$ nucleation, successfully achieving the ideal Li$_2$O$_2$ morphologies.

$$O_2 + e^- + Li^+ \rightarrow LiO_2 \tag{4}$$

$$2LiO_{2(sol)} \rightarrow Li_2O_2 + O_2 \tag{5}$$

$$LiO_2 * + Li^+ + e^- \rightarrow Li_2O_2 * \tag{6}$$

4 Conclusions

In summary, ZIF-67 as a template was used to synthesize 1T/2H-MCS composites via one-pot hydrothermal method with two-step temperature-raising process, which served as efficient bifunctional electrocatalysts for LOBs. It is evident that 1T/2H-MCS cathodes display extraordinary electrochemical properties, including high reversible discharge/charge specific capacities of 18,721/18,500 mAh g^{-1} at 100 mA g^{-1} and ultralong cycle life of 2420 h at 100 mA g^{-1} under a cutoff specific capacity of 1000 mAh g^{-1}. When applied in pouch-type LOBs, 1T/2H-MCS cathodes exhibit an impressive and promising potential for practical applications. Based on DFT calculations and experimental results, it is proposed that significantly improved OER/ORR performance of 1T/2H-MCS cathodes is owing to the complementary effects of double heterojunctions derived from the charge donation form Co to Mo ions. Firstly, 1T-MoS$_2$@Co$_3$S$_4$ provided unblocked electron transport channels of Co–S–Mo bonds, well redistributing electrons within 1T/2H-MCS and hence significantly improving its interfacial electron transfer kinetics and electrocatalytic activities. Then, 2H-MoS$_2$@Co$_3$S$_4$ possesses a moderate antibonding orbital occupancy when absorbed oxygen-containing intermediates, optimizing the morphology of discharge product and accelerating their decomposition by modulating the adsorption energy. Furthermore, 1T/2H-MCS holds a dodecahedral hollow structure inherited from ZIF-67 and is decorated with MoS$_2$ nanosheets, which could restrict layer-oriented growth of MoS$_2$ and increase specific surface area to expose abundant stable active sites. This complementary relationship provides guidance for designing efficient electrocatalysts with double heterojunctions for LOBs.

Author Contributions Y. C. Dou and Z. Liu conducted experimental measurements and result analyses, as well as drafted the manuscript. J. Wang and L. L. Zhao conceived the research and polished the manuscript. X. A. Li, Z. Shang and L. Wang contributed to the theoretical model construction and DFT calculations. J. Zhang, F. P. Meng, Y. Liu, and Z. D. Zhang discussed the results and revised the manuscript. All authors commented and agreed on the final version.

Declarations

Supplementary Information The online version contains supplementary material available at https://doi.org/10.1007/s40820-025-01895-x.

References

1. X. Han, L. Zhao, J. Wang, Y. Liang, J. Zhang, Delocalized electronic engineering of Ni5P4 nanoroses for durable Li–O$_2$ batteries. Adv. Mater. **35**(35), 2301897 (2023). https://doi.org/10.1002/adma.202301897

2. P.G. Bruce, S.A. Freunberger, L.J. Hardwick, J.-M. Tarascon, Li–O$_2$ and Li–S batteries with high energy storage. Nat. Mater. **11**(1), 19–29 (2012). https://doi.org/10.1038/nmat3191

3. L. Ma, T. Yu, E. Tzoganakis, K. Amine, T. Wu et al., Fundamental understanding and material challenges in rechargeable nonaqueous Li–O$_2$ batteries: recent progress and perspective. Adv. Energy Mater. **8**(22), 1800348 (2018). https://doi.org/10.1002/aenm.201800348

4. Y. Zhou, S. Guo, Recent advances in cathode catalyst architecture for lithium–oxygen batteries. eScience **3**(4), 100123 (2023). https://doi.org/10.1016/j.esci.2023.100123

5. T. Jian, W. Ma, C. Xu, H. Liu, J. Wang, Intermetallic-driven highly reversible electrocatalysis in Li–CO$_2$ battery over nanoporous Ni$_3$Al/Ni heterostructure. eScience **3**(3), 100114 (2023). https://doi.org/10.1016/j.esci.2023.100114

6. G. Yue, Z. Hong, Y. Xia, T. Yang, Y. Wu, Bifunctional electrocatalysts materials for non-aqueous Li–air batteries. Coatings **12**(8), 1227 (2022). https://doi.org/10.3390/coatings12081227

7. N. Sahu, J.N. Behera, MOF-derived Co$_3$S$_4$ nanoparticles embedded in nitrogen-doped carbon for electrochemical oxygen production. ACS Appl. Nano Mater. **6**(9), 7686–7693 (2023). https://doi.org/10.1021/acsanm.3c00845

8. M. Chauhan, K.P. Reddy, C.S. Gopinath, S. Deka, Copper cobalt sulfide nanosheets realizing a promising electrocatalytic oxygen evolution reaction. ACS Catal. **7**(9), 5871–5879 (2017). https://doi.org/10.1021/acscatal.7b01831

9. Y. Liu, C. Xiao, M. Lyu, Y. Lin, W. Cai et al., Ultrathin Co$_3$S$_4$ nanosheets that synergistically engineer spin states and exposed polyhedra that promote water oxidation under neutral conditions. Angew. Chem. **127**(38), 11383–11387 (2015). https://doi.org/10.1002/ange.201505320

10. Q. Wang, H. Xu, X. Qian, G. He, H. Chen, Sulfur vacancies engineered self-supported Co$_3$S$_4$ nanoflowers as an efficient bifunctional catalyst for electrochemical water splitting. Appl. Catal. B Environ. **322**, 122104 (2023). https://doi.org/10.1016/j.apcatb.2022.122104

11. B. Yang, C. Gu, Q. Zhao, G. Zhou, L. Xu et al., Reactive template-engaged synthesis of Ni-doped Co$_3$S$_4$ hollow and porous nanospheres with optimal electronic modulation toward high-efficiency electrochemical oxygen evolution. Inorg. Chem. Front. **9**(15), 3924–3932 (2022). https://doi.org/10.1039/D2QI00896C

12. X. Wang, M. Yu, X. Feng, Electronic structure regulation of noble metal-free materials toward alkaline oxygen electrocatalysis. eScience **3**(4), 100141 (2023). https://doi.org/10.1016/j.esci.2023.100141

13. L. Bo, W. Shi, F. Nian, Y. Hu, L. Pu et al., Interface engineering of Co$_3$S$_4$@Co$_3$O$_4$/N, S-doped carbon core@shell nanostructures serve as an excellent bifunctional ORR/OER electrocatalyst for rechargeable Zn-air battery. Sep. Purif. Technol. **307**, 122536 (2023). https://doi.org/10.1016/j.seppur.2022.122536

14. S. Kumar, R. Kumar, N. Goyal, A. Vazhayil, A. Yadav et al., N-doped carbon nanotubes nucleated through cobalt nanoparticles as bifunctional catalysts for zinc–air batteries. ACS Appl. Nano Mater. **7**(7), 7865–7882 (2024). https://doi.org/10.1021/acsanm.4c00479

15. H. He, D. Huang, Q. Gan, J. Hao, S. Liu et al., Anion vacancies regulating endows MoSSe with fast and stable potassium ion storage. ACS Nano **13**(10), 11843–11852 (2019). https://doi.org/10.1021/acsnano.9b05865

16. S. Zhang, L. Sun, L. Yu, G. Zhai, L. Li et al., Core–shell CoSe$_2$/WSe$_2$ heterostructures@carbon in porous carbon nanosheets as advanced anode for sodium ion batteries. Small **17**(49), 2103005 (2021). https://doi.org/10.1002/smll.202103005

17. G. Zhang, H. Liu, J. Qu, J. Li, Two-dimensional layered MoS$_2$: rational design, properties and electrochemical applications. Energy Environ. Sci. **9**(4), 1190–1209 (2016). https://doi.org/10.1039/c5ee03761a

18. D. Tan, M. Willatzen, Z.L. Wang, Prediction of strong piezoelectricity in 3R-MoS$_2$ multilayer structures. Nano Energy **56**, 512–515 (2019). https://doi.org/10.1016/j.nanoen.2018.11.073

19. R. Suzuki, M. Sakano, Y.J. Zhang, R. Akashi, D. Morikawa et al., Valley-dependent spin polarization in bulk MoS$_2$ with broken inversion symmetry. Nat. Nanotechnol. **9**(8), 611–617 (2014). https://doi.org/10.1038/nnano.2014.148

20. A. Hu, J. Long, C. Shu, R. Liang, J. Li, Three-dimensional interconnected network architecture with homogeneously dispersed carbon nanotubes and layered MoS$_2$ as a highly efficient cathode catalyst for lithium-oxygen battery. ACS Appl. Mater. Interfaces **10**(40), 34077–34086 (2018). https://doi.org/10.1021/acsami.8b06912

21. Z.-L. Wang, D. Xu, J.-J. Xu, L.-L. Zhang, X.-B. Zhang, Graphene oxide gel-derived, free-standing, hierarchically porous carbon for high-capacity and high-rate rechargeable Li-O$_2$ batteries. Adv. Funct. Mater. **22**(17), 3699–3705 (2012). https://doi.org/10.1002/adfm.201200403

22. X. Wang, Y. Li, X. Bi, L. Ma, T. Wu et al., Hybrid li-ion and li-O$_2$ battery enabled by oxyhalogen-sulfur electrochemistry. Joule **2**(11), 2381–2392 (2018). https://doi.org/10.1016/j.joule.2018.07.019

23. A. Hu, C. Shu, X. Qiu, M. Li, R. Zheng et al., Improved cyclability of lithium–oxygen batteries by synergistic catalytic effects of two-dimensional MoS$_2$ nanosheets anchored on hollow carbon spheres. ACS Sustainable Chem. Eng. **7**(7), 6929–6938 (2019). https://doi.org/10.1021/acssuschemeng.8b06496

24. X. Cao, Z. Chen, N. Wang, Z. Han, X. Zheng et al., Defected molybdenum disulfide catalyst engineered by nitrogen doping for advanced lithium–oxygen battery. Electrochim. Acta **383**, 138369 (2021). https://doi.org/10.1016/j.electacta.2021.138369

25. X. Cao, Y. Zhang, C. Lu, K. Fang, L. Chen et al., Synergistic dual atomic sites with localized electronic modulation enable high-performance lithium–oxygen batteries. Chem. Eng. J. **466**, 143351 (2023). https://doi.org/10.1016/j.cej.2023.143351

26. F. Gong, S. Ye, M. Liu, J. Zhang, L. Gong et al., Boosting electrochemical oxygen evolution over yolk-shell structured O-MoS$_2$ nanoreactors with sulfur vacancy and decorated Pt nanoparticles. Nano Energy **78**, 105284 (2020). https://doi.org/10.1016/j.nanoen.2020.105284

27. Z. Sun, J. He, M. Yuan, L. Lin, Z. Zhang et al., Li$^+$-clipping for edge S-vacancy MoS$_2$ quantum dots as an efficient

bifunctional electrocatalyst enabling discharge growth of amorphous Li_2O_2 film. Nano Energy **65**, 103996 (2019). https://doi.org/10.1016/j.nanoen.2019.103996

28. Y. Huang, Y. Sun, X. Zheng, T. Aoki, B. Pattengale et al., Atomically engineering activation sites onto metallic 1T-MoS_2 catalysts for enhanced electrochemical hydrogen evolution. Nat. Commun. **10**(1), 982 (2019). https://doi.org/10.1038/s41467-019-08877-9

29. Q.H. Wang, K. Kalantar-Zadeh, A. Kis, J.N. Coleman, M.S. Strano, Electronics and optoelectronics of two-dimensional transition metal dichalcogenides. Nat. Nanotechnol. **7**(11), 699–712 (2012). https://doi.org/10.1038/nnano.2012.193

30. G. Eda, T. Fujita, H. Yamaguchi, D. Voiry, M. Chen et al., Coherent atomic and electronic heterostructures of single-layer MoS_2. ACS Nano **6**(8), 7311–7317 (2012). https://doi.org/10.1021/nn302422x

31. S. Feng, J.R. Lunger, J.A. Johnson, Y. Shao-Horn, Hot lithium-oxygen batteries charge ahead. Science **361**(6404), 758 (2018). https://doi.org/10.1126/science.aau4792

32. S.S. Chou, N. Sai, P. Lu, E.N. Coker, S. Liu et al., Understanding catalysis in a multiphasic two-dimensional transition metal dichalcogenide. Nat. Commun. **6**, 8311 (2015). https://doi.org/10.1038/ncomms9311

33. Y. Feng, T. Zhang, J. Zhang, H. Fan, C. He et al., 3D 1T-MoS_2/CoS_2 heterostructure *via* interface engineering for ultrafast hydrogen evolution reaction. Small **16**(33), 2002850 (2020). https://doi.org/10.1002/smll.202002850

34. S.M. Abdel-Azim, M.M. Younus, A.S. Dhmees, M. Pannipara, S. Wageh et al., Facile synthesis of ZnS/1T-2H MoS_2 nanocomposite for boosted adsorption/photocatalytic degradation of methylene blue under visiblelight. Environ. Sci. Pollut. Res. Int. **29**(57), 86825–86839 (2022). https://doi.org/10.1007/s11356-022-21255-1

35. D. Wang, X. Zhang, S. Bao, Z. Zhang, H. Fei et al., Phase engineering of a multiphasic 1T/2H MoS_2 catalyst for highly efficient hydrogen evolution. J. Mater. Chem. A **5**(6), 2681–2688 (2017). https://doi.org/10.1039/C6TA09409K

36. Z. Zhou, L. Zhao, J. Wang, Y. Zhang, Y. Li et al., Optimizing *eg* orbital occupancy of transition metal sulfides by building internal electric fields to adjust the adsorption of oxygenated intermediates for $Li-O_2$ batteries. Small **19**(41), 2302598 (2023). https://doi.org/10.1002/smll.202302598

37. Z. Lei, J. Zhan, L. Tang, Y. Zhang, Y. Wang, Recent development of metallic (1T) phase of molybdenum disulfide for energy conversion and storage. Adv. Energy Mater. **8**(19), 1703482 (2018). https://doi.org/10.1002/aenm.201703482

38. C.-H. Li, C.-Z. Yuan, X. Huang, H. Zhao, F. Wu et al., Tailoring the electron redistribution of RuO_2 by constructing a Ru-O-La asymmetric configuration for efficient acidic oxygen evolution. eScience **5**(1), 100307 (2025). https://doi.org/10.1016/j.esci.2024.100307

39. D.W. Kim, J. Kim, J.H. Choi, D.H. Jung, J.K. Kang, Trifunctional graphene-sandwiched heterojunction-embedded layered lattice electrocatalyst for high performance in Zn-air battery-driven water splitting. Adv. Sci. **11**(42), 2408869 (2024). https://doi.org/10.1002/advs.202408869

40. O. Peng, R. Shi, J. Wang, X. Zhang, J. Miao et al., Hierarchical heterostructured nickle foam–supported Co_3S_4 nanorod arrays embellished with edge-exposed MoS_2 nanoflakes for enhanced alkaline hydrogen evolution reaction. Mater. Today Energy **18**, 100513 (2020). https://doi.org/10.1016/j.mtener.2020.100513

41. J. Sun, Z. Zhang, G. Lian, Y. Li, L. Jing et al., Electron-injection and atomic-interface engineering toward stabilized defected 1T-rich MoS_2 as high rate anode for sodium storage. ACS Nano **16**(8), 12425–12436 (2022). https://doi.org/10.1021/acsnano.2c03623

42. S. Wang, D. Zhang, B. Li, C. Zhang, Z. Du et al., Ultrastable in-plane 1T–2H MoS_2 heterostructures for enhanced hydrogen evolution reaction. Adv. Energy Mater. **8**(25), 1801345 (2018). https://doi.org/10.1002/aenm.201801345

43. S. Kim, O. Kwon, C. Kim, O. Gwon, H.Y. Jeong et al., Strategy for enhancing interfacial effect of bifunctional electrocatalyst: infiltration of cobalt nanooxide on perovskite. Adv. Mater. Interfaces **5**(12), 1800123 (2018). https://doi.org/10.1002/admi.201800123

44. J. Suntivich, K.J. May, H.A. Gasteiger, J.B. Goodenough, Y. Shao-Horn, A perovskite oxide optimized for oxygen evolution catalysis from molecular orbital principles. Science **334**(6061), 1383–1385 (2011). https://doi.org/10.1126/science.1212858

45. J. Suntivich, H.A. Gasteiger, N. Yabuuchi, H. Nakanishi, J.B. Goodenough et al., Design principles for oxygen-reduction activity on perovskite oxide catalysts for fuel cells and metal-air batteries. Nat. Chem. **3**(7), 546–550 (2011). https://doi.org/10.1038/nchem.1069

46. G. Zhang, H. Yu, X. Li, X. Zhang, C. Hou et al., Construction of MnS/MoS_2 heterostructure on two-dimensional MoS_2 surface to regulate the reaction pathways for high-performance $Li-O_2$ batteries. J. Energy Chem. **93**, 443–452 (2024). https://doi.org/10.1016/j.jechem.2024.01.076

47. Y. Xia, T. Yang, Z. Wang, T. Mao, Z. Hong et al., Van der Waals forces between S and P ions at the CoP-C@MoS_2/C heterointerface with enhanced lithium/sodium storage. Adv. Funct. Mater. **33**(35), 2302830 (2023). https://doi.org/10.1002/adfm.202302830

48. X. Li, Y. Sun, J. Xu, Y. Shao, J. Wu et al., Selective visible-light-driven photocatalytic CO_2 reduction to CH_4 mediated by atomically thin $CuIn_5S_8$ layers. Nat. Energy **4**(8), 690–699 (2019). https://doi.org/10.1038/s41560-019-0431-1

49. X. Wang, Y. Zhang, H. Si, Q. Zhang, J. Wu et al., Single-atom vacancy defect to trigger high-efficiency hydrogen evolution of MoS_2. J. Am. Chem. Soc. **142**(9), 4298–4308 (2020). https://doi.org/10.1021/jacs.9b12113

50. X. Han, L. Zhao, Y. Liang, J. Wang, Y. Long et al., Interfacial electron redistribution on lattice-matching NiS_2/$NiSe_2$ homologous heterocages with dual-phase synergy to tune the formation routes of Li_2O_2. Adv. Energy Mater. **12**(47), 2202747 (2022). https://doi.org/10.1002/aenm.202202747

51. W. Song, S. Zhou, S. Hu, W. Lai, Y. Lian et al., Surface engineering of CoMoS nanosulfide for hydrodeoxygenation of

lignin-derived phenols to arenes. ACS Catal. **9**(1), 259–268 (2019). https://doi.org/10.1021/acscatal.8b03402

52. J. Liu, Y. Zhao, X. Li, C. Wang, Y. Zeng et al., CuCr$_2$O$_4$@ rGO nanocomposites as high-performance cathode catalyst for rechargeable lithium-oxygen batteries. Nano-Micro Lett. **10**(2), 22 (2018). https://doi.org/10.1007/s40820-017-0175-z

53. X. Geng, W. Sun, W. Wu, B. Chen, A. Al-Hilo et al., Pure and stable metallic phase molybdenum disulfide nanosheets for hydrogen evolution reaction. Nat. Commun. **7**, 10672 (2016). https://doi.org/10.1038/ncomms10672

54. M.-Q. Wang, C. Ye, S.-J. Bao, Z.-Y. Chen, H. Liu et al., Ternary Ni$_x$Co$_{3−x}$S$_4$ with a fine hollow nanostructure as a robust electrocatalyst for hydrogen evolution. ChemCatChem **9**(22), 4169–4174 (2017). https://doi.org/10.1002/cctc.201700935

55. Y. Xia, Z. Hong, L. Wang, X. Jin, S. Lin et al., Constructing the double oxygen vacancy in Ni-doped Co$_3$O$_4$ to enhance the electrochemical performance in lithium-oxygen batteries. J. Power. Sources **635**, 236542 (2025). https://doi.org/10.1016/j.jpowsour.2025.236542

56. X. Chen, Y. Zhang, C. Chen, H. Li, Y. Lin et al., Atomically dispersed ruthenium catalysts with open hollow structure for lithium-oxygen batteries. Nano-Micro Lett. **16**(1), 27 (2023). https://doi.org/10.1007/s40820-023-01240-0

57. Y. Xia, L. Wang, G. Gao, T. Mao, Z. Wang et al., Constructed Mott-schottky heterostructure catalyst to trigger interface disturbance and manipulate redox kinetics in Li-O$_2$ battery. Nano-Micro Lett. **16**(1), 258 (2024). https://doi.org/10.1007/s40820-024-01476-4

58. C.A.F. Nason, A.P. Vijaya Kumar Saroja, Y. Lu, R. Wei, Y. Han et al., Layered potassium titanium niobate/reduced graphene oxide nanocomposite as a potassium-ion battery anode. Nano-Micro Lett. **16**(1), 1 (2023). https://doi.org/10.1007/s40820-023-01222-2

59. T. Yang, Y. Xia, T. Mao, Q. Ding, Z. Wang et al., Phosphorus vacancies and heterojunction interface as effective lithium-peroxide promoter for long-cycle life lithium–oxygen batteries. Adv. Funct. Mater. **32**(49), 2209876 (2022). https://doi.org/10.1002/adfm.202209876

60. S. Ma, Y. Wu, J. Wang, Y. Zhang, Y. Zhang et al., Reversibility of noble metal-catalyzed aprotic Li-O$_2$ batteries. Nano Lett. **15**(12), 8084–8090 (2015). https://doi.org/10.1021/acs.nanolett.5b03510

61. T. Bai, J. Wang, H. Zhang, F. Ji, W. Song et al., Atomic Ni-catalyzed cathode and stabilized Li metal anode for high-performance Li–O$_2$ batteries. eScience **5**(1), 100310 (2025). https://doi.org/10.1016/j.esci.2024.100310

62. Z. Lian, Y. Lu, S. Zhao, Z. Li, Q. Liu, Engineering the electronic interaction between atomically dispersed Fe and RuO$_2$ attaining high catalytic activity and durability catalyst for Li-O$_2$ battery. Adv. Sci. **10**(9), 2205975 (2023). https://doi.org/10.1002/advs.202205975

63. S. Guan, X. Li, Y. Zhao, G. Han, S. Lou et al., Single-atom tailored transition metal oxide enhances d-p hybridization in catalytic conversion for lithium-oxygen batteries. Chem. Eng. J. **488**, 151064 (2024). https://doi.org/10.1016/j.cej.2024.151064

64. Q. Lv, Z. Zhu, Y. Ni, J. Geng, F. Li, Spin-state manipulation of two-dimensional metal–organic framework with enhanced metal–oxygen covalency for lithium-oxygen batteries. Angew. Chem. Int. Ed. **61**(8), e202114293 (2022). https://doi.org/10.1002/anie.202114293

65. A.J. Medford, A. Vojvodic, J.S. Hummelshøj, J. Voss, F. Abild-Pedersen et al., From the Sabatier principle to a predictive theory of transition-metal heterogeneous catalysis. J. Catal. **328**, 36–42 (2015). https://doi.org/10.1016/j.jcat.2014.12.033

66. J. Tian, Y. Rao, W. Shi, J. Yang, W. Ning et al., Sabatier relations in electrocatalysts based on high-entropy alloys with wide-distributed d-band centers for Li-O$_2$ batteries. Angew. Chem. Int. Ed. **62**(44), e202310894 (2023). https://doi.org/10.1002/anie.202310894

67. Y. Liu, J. Cai, J. Zhou, Y. Zang, X. Zheng et al., Tailoring the adsorption behavior of superoxide intermediates on nickel carbide enables high-rate Li–O$_2$ batteries. eScience **2**(4), 389–398 (2022). https://doi.org/10.1016/j.esci.2022.06.002